Allosteric Gain-of-Function and Off-Mechanism Effects of ATP-Competitive Kinase Inhibitors Revealed by Multimodal Proteomics

Viviane Reber (1), Sabrina Keller (1), Stefanie A. Loosli (1), Yumi Arima (2), Tatjana Kleele (2), Paola Picotti (1), Matthias Gstaiger (1)

1 Institute of Molecular Systems Biology, Department of Biology, ETH Zurich, Zurich, Switzerland

2 Institute of Biochemistry, Department of Biology, ETH Zurich, Zurich, Switzerland

Corresponding author: Matthias Gstaiger, matthias.gstaiger@imsb.biol.ethz.ch

Abstract

Protein kinases are critical regulators of cellular processes, and their dysregulation is a common hallmark of human disorders. While ATP-competitive inhibitors are the primary therapeutic strategy to block aberrant kinase activity, it is largely unknown how their binding could affect non-catalytic kinase functions via changes in kinase conformation and protein-protein interactions (PPIs). Here, we introduce a multimodal proteomics approach to systematically characterize these overlooked effects, providing a crucial framework for comprehensive target engagement analysis. Our integrated platform, which combines affinity purification coupled with limited proteolysis mass spectrometry (AP-LiP-MS), AP-MS and *in vivo* proximity labelling, enables comprehensive exploration of inhibitor-induced allosteric and non-catalytic functional changes. Using this pipeline, we discovered that all four kinases analyzed (DCLK1, CAMKK2, CHEK1, and PRKCA) undergo structural rearrangements upon inhibitor binding in the autoinhibitory domain (AID) and other regions. These structural shifts underlie changes in complex formation, membrane association and other non-catalytic functions. Our work suggests that these on-target, off-mechanism effects are highly prevalent and provides the analytical tools to systematically characterize a frequently overlooked phenomenon highly relevant for understanding drug side effects to guide the development of novel therapeutics.

Introduction

The functional landscape of a protein is shaped by the interdependent relationship of its conformation, post-translational modifications (PTMs), and multiple interactions with other proteins and small molecules. Tight regulation is essential for control of virtually all cellular processes. Genetic mutations and changes in signaling context that affect protein function are often causally linked to the development of human diseases[1,2]. Highly specific small molecule modulators of protein function, also referred to as chemical probes, provide unique opportunities for the control of protein function for pharmacological intervention and basic research, and several ongoing initiatives aim to develop chemical probes against all human proteins[3]. One of the largest groups of proteins targeted by clinically relevant probes are protein kinases[4,5]. Most probes targeting kinases inhibit their catalytic activity in an ATP-competitive manner.

Several reports have demonstrated that these inhibitors unexpectedly activate non-catalytic kinase functions through alternative mechanisms, causing unintended phenotypes. One prominent example is the type I BRAF inhibitor GDC-0879, which paradoxically causes activation of downstream mitogen-activated protein kinase (MAPK) signaling and cell proliferation via a mechanism promoting dimerization between BRAF and CRAF[6,7]. Other known examples include inhibitors against RAC-alpha serine/threonine-protein kinase (AKT1)[8] and c-ABL[9]. Such mechanisms often escape classical target engagement analyses that focus on kinetic parameters, probe specificity and structural characterization of the probe-kinase domain (KD) interaction. As a result, such allosteric modalities are frequently discovered serendipitously only at late stages, after probe development has been completed.

Characterization of non-catalytic mechanisms often requires additional analysis of changes in kinase structure and protein-protein interactions (PPIs). Beyond the catalytic core, the 518 members of the human protein kinase family[10] contain multiple additional domains that confer diverse biochemical properties such as additional enzymatic activities or complex formation, which are key for correct kinase function[11,12]. However, previous structural analyses often used highly purified, and usually

truncated, recombinant proteins which lack key interaction partners, PTMs and domains. Additionally, current methods used to characterize changes in PPIs, such as X-ray crystallography, or downstream phosphorylation events, such as western blots, rely heavily on previous knowledge about affected proteins and signaling networks, and therefore do not allow de novo discovery of such mechanisms. We therefore developed an unbiased proteomics-based analytical strategy to systematically monitor allosteric dynamic and complex remodeling following compound binding.

We adapted and employed limited proteolysis coupled with mass spectrometry (LiP-MS) on affinity purified (AP) samples (AP-LiP-MS) to study structural changes based on conformation dependent protease cleavage patterns[13] at high sequence coverage. We combined AP-LiP-MS with contextual proteomics, using both AP-MS[12] and *in vivo* proximity labeling[14] to better understand how conformation and biochemical context of target kinases may control non-catalytic roles of kinases following inhibitor binding[15]. The combination of these methods provides detailed insights on structural and PPI changes, enabling the discovery of new mechanisms of action.

We applied our workflow to study changes in conformation and interactions of kinases with autoinhibitory domains (AIDs). Autoinhibition directly regulates conformation and accessibility of the ATP-binding sites through domain-domain interactions (DDIs), affecting both kinase activity and interactions with substrates[16,17]. However, it remains unclear how these regulatory mechanisms are affected by inhibitor binding. Additionally, investigating structural changes in AIDs remains a technical challenge as many are disordered[18,19] or linked to the KD via a disordered linker[20], and therefore cannot easily be resolved using static structural methods. Our workflow is thus uniquely suited to capture these changes.

First, we demonstrated that AP-LiP-MS successfully captured known structural changes in Doublecortin-like kinase 1 (DCLK1) prior to applying our workflow to Calcium/calmodulin-dependent protein kinase kinase 2 (CAMKK2), Checkpoint kinase 1 (CHEK1) and Protein kinase C alpha (PRKCA). For all kinases, we identified structural changes in the AID upon binding of ATP-competitive probes that are consistent with a transition from a closed to an open, active-like conformation characterized

by dissociation of the DDI between the KD and AID. We subsequently analyzed how this change in protein conformation alters the regulation of other kinase functions. We found that compound binding can substantially affect PPIs and kinase localization independent of catalytic inhibition, information that is essential for modelling non-canonical phenotypic responses. Our results suggest that these mechanisms are highly prevalent among kinases with AIDs.

Our workflow is not restricted to kinase targets but can also be used to study other protein classes. This offers a powerful analytical strategy to research non-catalytic protein functions, systematically characterize off-mechanism effects of known compounds and to identify new classes of compounds which can control non-catalytic protein function via allosteric changes and target complex formation.

Results

Capturing allosteric changes in protein kinases upon inhibitor binding using AP-LiP-MS

We developed a method to monitor probe-induced structural changes in protein kinases with increased protein coverage. The method is based on our previous work demonstrating that LiP-MS can detect structural changes associated with small molecule binding[21]. LiP-MS relies on the generation of conformation specific protein fragments by the protease proteinase K (PK), which preferentially cleaves accessible and flexible regions[13]. Perturbations that alter protein accessibility or flexibility lead to changes in PK cleavage patterns, resulting in differential peptide abundance. The sensitivity of detecting these structural changes critically depends on protein sequence coverage, which can limit the analysis of low-abundance proteins such as kinases in complex cell lysates[21]. While previous studies have used purified recombinant proteins to address this limitation[22,23], this approach does not fully capture the native context of the protein since it lacks physiological PTMs and complex partners essential for correct structure and function. Therefore, we developed AP-LiP-MS by performing LiP-MS on native AP eluates (Fig. 1a). In this approach, target proteins are purified from human cells under

native conditions and treated with an inhibitor, prior to the LiP-step with PK. Samples are then digested with trypsin and analyzed by liquid chromatography coupled mass spectrometry (LC-MS).

We selected the serine/threonine-protein kinase DCLK1 to benchmark our approach, since X-ray crystal structures are available for both the inhibitor-bound and unbound protein (Fig. 1b). These structures revealed an autoinhibited configuration for DCLK1 in which the AID occupies the ATP-binding pocket[24]. This pocket is also the binding site for the recently developed inhibitor DCLK1-IN-1[25,26]. Although the AID is absent in the inhibitor-bound structural model due to a truncated protein being used for crystallography, we infer that the inhibitor must displace the AID to avoid steric clashes, especially given its nanomolar binding affinity[25]. We asked if AP-LiP-MS would be able to capture such structural changes associated with a transition between these states upon treatment with DCLK1-IN-1.

AP-LiP-MS profiling of DCLK1 quantified a total of 13150 peptides of which 367 peptides mapped to DCLK1, resulting in 75.4% sequence coverage. We only found 29 peptides with significantly altered intensity, 25 of which were DCLK1 peptides, clearly indicating structural changes in DCLK1 upon inhibitor binding (Fig. 1c, Supplementary Fig. 1a). Strikingly, all 25 peptides mapped exclusively to the AID of DCLK1 (Fig. 1d). These peptides are half-tryptic, meaning that one end was generated by PK cleavage. The increased abundance of these peptides indicates increased PK susceptibility and thus increased accessibility of the AID. This observation strongly supports an inhibitor-induced disruption of the AID-KD interaction and a transition from an autoinhibited to an open conformation as anticipated from X-ray structures.

In summary, we have developed a robust method to probe inhibitor-induced structural changes across the entire sequence of a kinase. We resolved changes in the flexible AID, which is challenging to resolve using traditional structural biology techniques. Consistent with resolved structures, we propose that DCLK1-IN-1 binding induces a DDI change between the AID and the KD of DCLK1.

Inhibitor binding causes allosteric changes in kinase autoinhibitory domains

To determine whether AID rearrangement upon inhibitor binding is a more general phenomenon, we extended our analysis to additional kinases with diverse AIDs that vary in both structure and regulatory mechanism, and for which well-characterized ATP-competitive inhibitors are available. We therefore selected CAMKK2, CHEK1, and PRKCA as model kinases, representing distinct modes of autoinhibition and regulatory control. The AID of CAMKK2 is a small linear motif and binds the back of the KD[27]. Activation occurs through binding of calmodulin to the AID, which relieves the interaction between the AID and the KD. CHEK1 instead has a larger, structured AID. Its activation is triggered via phosphorylation from the upstream kinase Ataxia telangiectasia and Rad3 related (ATR), which relieves the interaction between the AID and the KD of CHEK1[28]. On the other hand, PRKCA has an N-terminal disordered pseudosubstrate motif that dissociates from the KD upon Ca^{2+} binding[29,30]. For each of these kinases, specific high-affinity ATP-competitive inhibitors have been developed: SGC-CAMKK2-1 for CAMKK2[31], rabusertib for CHEK1[32], and Gö 6983 for PRKCA[33].

We applied AP-LiP-MS to CAMKK2, CHEK1 and PRKCA to investigate the structural consequences of inhibitor binding. For all three kinases we observed a structural change at the AID upon binding of the respective inhibitor (Fig. 1e, Supplementary Fig. 1b-g). Similar to DCLK1, CAMKK2 showed changes exclusively in its AID that were consistent with increased PK susceptibility. In contrast, CHEK1 and PRKCA also underwent structural alterations throughout the KD. Additionally, the PRKCA inhibitor Gö 6983 led to structural changes in the C2-domain. We observed increased PK accessibility of both domains, potentially reflecting an allosteric disruption of the C2-KD interaction which has been reported for other PRKCA inhibitors[34]. Notably, all observed structural changes upon inhibitor treatment occurred in the same regions previously described to be involved in kinase activation. Specifically, the AID is known to dissociate from the KD upon activation for all investigated kinases[27,35-37]. Furthermore, PRKCA activation is also associated with larger rearrangements in its membrane-binding C1 and C2 domains[38]. These results suggest that kinases undergo conformational changes upon inhibitor binding in regions typically associated with their activation.

Overall, we observed that ATP-competitive inhibitors induced structural changes at the AID of all tested kinases, leading to a shift in the distribution of kinase structural states. As the structural changes occurred in regions previously described to be involved in kinase activation, we propose that inhibitor binding causes a transition from an autoinhibited state to an open, active-like conformation.

Formation of the CAMKK2-PRKAA1 complex upon CAMKK2 inhibition inhibits PRKAA1 phosphorylation by other kinases

An open kinase conformation induced by inhibitor binding could expose interaction surfaces hidden in the autoinhibited conformation[39]. We therefore applied AP-MS (Fig. 2a) and *in vivo* proximity labeling (Fig. 2b) to profile subsequent changes in kinase complexes and proximity, respectively.

We first measured changes in CAMKK2 complex formation. AP-MS identified 66 interactors of CAMKK2 across all treatments, 22 of which were previously listed in the BioGrid database[40] (Supplementary Table 1). Five proteins changed in abundance in response to SGC-CAMKK2-1 (Fig. 2c, Supplementary Fig. 2a, b). 5'-AMP-activated protein kinase subunit alpha-1 (PRKAA1), the catalytic subunit of the trimeric AMPK complex and known substrate[41] and interactor[42] of CAMKK2, was the most strongly increased protein in CAMKK2 complexes in the presence of the inhibitor. Extended synaptotagmin-2 (ESYT2), another known CAMKK2 interactor, was also increased but to a lesser extent than PRKAA1. We also found three proteins whose interaction was reduced upon inhibitor binding. This includes a strong reduction of Obscurin-like protein 1 (OBSL1), a known CAMKK2 interaction albeit of unknown function and, with lower significance, the reduced abundance of metabolic enzyme ATP-dependent 6-phosphofructokinase (PFKM) and the Puromycin-sensitive aminopeptidase (NPEPPS).

To explore changes in the interaction landscape of CAMKK2 *in vivo*, we extended our analysis by proximity labeling using miniTurbo-CAMKK2 expressing cells (Fig. 2d, Supplementary Fig. 2c, d). We found 71 proteins with altered proximity to CAMKK2 in the presence of the inhibitor. Gene ontology (GO) enrichment analysis revealed that SGC-CAMKK2-1 caused changes in proximity to proteins related to actin filament organization and metabolic processes (Fig. 2e). Among these proteins were five

subunits of the trimeric AMPK complex as well as known AMPK interactors, such as TP53 (Fig. 2f). The increased proximity to catalytic as well as regulatory AMPK subunits suggests complex formation between CAMKK2 and trimeric AMPK complexes upon SGC-CAMKK2-1 treatment. Interestingly, since the CAMKK2-PRKAA1 interaction has been previously observed only in the presence of Ca^{2+}, calmodulin and ATP, this interaction likely requires an active CAMKK2 conformation[43]. Thus, our observation that CAMKK2 binds AMPK upon inhibition with SGC-CAMKK2-1 is consistent with the AP-LiP-MS data which suggested that the inhibitor stabilizes an open, active-like kinase conformation.

Reassuringly, SGC-CAMKK2-1 also induced a strong increase of endogenous CAMKK2 in the proximity of PRKAA1 following inhibitor treatment upon reciprocal *in vivo* proximity labeling using miniTurbo-PRKAA1 expressing cells (Fig. 2g, Supplementary Fig. 2e, f), confirming our previous findings. SGC-CAMKK2-1 treatment also caused a remodeling of PRKAA1 interactions beyond CAMKK2 as we observed a significant enrichment for proteins linked to mitochondria and endoplasmic reticulum based on a GO enrichment analysis (Fig. 2h). This suggests that CAMKK2 inhibitors also change the biochemical environment of AMPK beyond stabilizing the CAMKK2-PRKAA1 interaction.

The inhibitor-induced CAMKK2-AMPK complex formation could be caused by the observed changes in CAMKK2 conformation but also result from decreased AMPK phosphorylation following catalytic inhibition of CAMKK2[31]. To disentangle the effects of catalytic inhibition and conformational change on the altered PPIs, we compared inhibitor-induced structural changes and complex formation between wildtype (WT) CAMKK2 and the following three mutants: the catalytically inactive D312A mutant[44], the R311C mutant found in patients with bipolar disorder[45], and the phosphomimetic mutation T483D, which is at the major autophosphorylation site of CAMKK2 associated with autonomous activity[46].

First, we applied AP-LiP-MS to compare structural changes between wildtype and mutant CAMKK2 following inhibitor treatment. We found that all tested mutants displayed a structural change at or close to the AID similar to wildtype CAMKK2 in response to SGC-CAMKK2-1 (Fig. 3a, Supplementary Fig. 3a-c) demonstrating that all mutants can bind the compound and respond with a conformational

change similar to WT CAMKK2. The structural change in the AID for the autonomously active CAMKK2 T483D mutant suggests that it is also in a closed conformation in the absence of the inhibitor. This is consistent with previous reports showing that activity of the CAMKK2 isoform used in our study depends on calmodulin binding also when autonomously active[47].

We subsequently analyzed CAMKK2-PRKAA1 complex formation across the mutants (Fig. 3b, Supplementary Fig. 3d-f). Upon SGC-CAMKK2-1 treatment, both the catalytically inactive D312A and the autonomously active T483D mutant displayed an interaction pattern with PRKAA1 similar to wildtype CAMKK2, suggesting that these changes are not linked to CAMKK2 catalytic activity but rather relate to the observed structural change. The CAMKK2 disease mutation R311C on the other hand completely abolished the interaction with PRKAA1, irrespective of inhibitor treatment, which could hint at a novel disease mechanism via uncoupling the CAMKK2-AMPK signaling axis in patients with this genetic disorder.

To better understand potential implications of CAMKK2-PRKAA1 complex formation, we generated a structural prediction of the two KDs using AlphaFold3[48] (Fig. 3c, Supplementary Fig. 3g, h). The KD of CAMKK2 is shown in blue and the KD of PRKAA1 is purple. The interaction interfaces are highlighted in light blue and pink, respectively. In the predicted PPI interface of CAMKK2, we observed that R311, shown in magenta, is oriented towards the predicted interaction interface, while D312, shown in yellow, is outside of the interaction interface (Fig. 3d). This suggests that the R311C mutation may negatively affect the integrity of the interaction interface needed for PRKAA1 binding and may explain why the SGC-CAMKK2-1-induced interaction with PRKAA1 is abolished for CAMKK2 R311C but not D312A.

We further investigated the predicted binding interface of PRKAA1 (Fig. 3e) and noticed that T183, shown in orange, is buried in the interface of the predicted CAMKK2-PRKAA1 complex. While this residue can be phosphorylated by CAMKK2 in response to increased intracellular Ca^{2+} ions, it is phosphorylated upon glucose starvation primarily by liver kinase B1 (LKB1) [49]. Since PRKAA1 is bound by CAMKK2 in response to SGC-CAMKK2-1, this site would become inaccessible to other upstream

kinases. This led us to hypothesize that formation of the CAMKK2-PRKAA1 complex would inhibit PRKAA1 T183 phosphorylation by other kinases such as LKB1. We tested this hypothesis by analyzing T183 phosphorylation in HEK293 cells subjected to glucose starvation and siRNA-mediated depletion of CAMKK2 (Fig. 3f, Supplementary Fig. 4). We found that the glucose-induced T183 phosphorylation of PRKAA1 was indeed decreased after CAMKK2 inhibition with SGC-CAMKK2-1. Importantly, this decrease was rescued upon siRNA-mediated knockdown of CAMKK2, supporting a model where SGC-CAMKK2-1 induced formation of CAMKK2-PRKAA1 complexes could block the T183 phosphorylation and activation of PRKAA1 by other kinases.

Taken together, we found that SGC-CAMKK2-1 causes structural changes and remodeling of CAMKK2-containing complexes, including a strong increase in CAMKK2-PRKAA1 complex formation. Consequently, probe treatment extensively altered the protein environment of PRKAA1. Our data thus show how an ATP-competitive kinase inhibitor can affect the biochemical context of both its target but also of associated signaling proteins. We showed that most inhibitor-induced changes in protein interactions cannot be simply explained by inhibition of catalytic activity, and that SGC-CAMKK2-1 can regulate a non-catalytic scaffolding function of CAMKK2 via conformational changes. The disease-associated mutant R311C fully blocked CAMKK2-PRKAA1 complex formation, representing first evidence for a potential molecular mechanism associated with bipolar disorder linked to this mutation and emphasizing the importance of genetic context for personalized drug response. Finally, we showed that SGC-CAMKK2-1 induces CAMKK2-AMPK complex formation, which may represent a novel mechanism to hinder PRKAA1 phosphorylation by other kinases. This finding underscores the importance of exploring inhibitor-induced PPI changes to broaden our understanding of multilayered target engagement mechanisms.

Rabusertib inhibits CHEK1 complex formation with the mitochondrial protein CLBP and causes mitochondrial fragmentation

AP-LiP-MS revealed significant structural alterations in the KD and the AID of CHEK1 upon binding of the inhibitor rabusertib. To understand how these changes may remodel the interactome of CHEK1, we performed AP-MS and *in vivo* proximity labeling experiments. AP-MS identified 51 interactors of CHEK1, of which 39 have been reported previously[40] (Supplementary Table 2). Rabusertib affected CHEK1 interactions with 18 proteins (Fig. 4a, Supplementary Fig. 5a) that upon GO enrichment analysis show clear enrichment for terms related to known CHEK1 functions in the DNA-damage response (Fig. 4b). This includes increased interaction with 14-3-3 proteins zeta (YWHAZ) and theta (YWHAQ), which has also been observed upon DNA damage-induced CHEK1 activation[50]. Inhibitor treatment in addition stabilized the interaction with Ubiquitin carboxyl-terminal hydrolase 7 (USP7), a deubiquitylating (DUB) enzyme known to directly interact with CHEK1[51]. USP7 has increased DUB activity towards CHEK1 upon DNA damage[52]. Moreover, rabusertib increased the abundance of CHEK1 complexes containing proliferating cell nuclear antigen (PCNA) and the DNA replication licensing factors MCM2, MCM3, MCM4, MCM5 and MCM6, which are subunits of the MCM complex. Both these interactions are required for CHEK1 activation[53,54]. These proteins are part of a highly interconnected PPI network (Fig. 4c). The only protein we found to dissociate from CHEK1 upon rabusertib treatment was the mitochondrial protein CLPB.

In vivo proximity labeling with miniTurbo-CHEK1 showed that rabusertib induced the proximity to 12 proteins with known functional links to CHEK1 (Fig. 4d, Supplementary Fig. 5b, c) including Aurora kinase A- and ninein-interacting protein (AUNIP), transcription factor E2F8, Rap1-interacting factor 1 (RIF1), MCM10, the kinases tousled-like 2 (TLK2) and ATR, and the scaffolding protein DNA topoisomerase 2-binding protein 1 (TOPBP1). ATR and TOPBP1 act upstream to activate CHEK1 by phosphorylation on multiple sites including S317 upon DNA damage[55].

We therefore analyzed the abundance of phosphopeptides in purified CHEK1 complexes, and observed increased phosphorylation of CHEK1 on the known ATR phosphorylation site S317 upon rabusertib treatment (Fig. 4e, Supplementary Fig. 5d). This paradoxical activating phosphorylation in response to CHEK1 inhibition has been noticed in the past and might be due to increased spontaneous DNA damage as observed previously for other CHEK1 inhibitors[56,57] (Supplementary Fig. 5e, 6). We also observed decreased CHEK1 autophosphorylation at S296 (Fig. 4e) in rabusertib-treated cells as expected upon CHEK1 catalytic inhibition[58]. These phosphorylation changes might explain both the enhanced 14-3-3 protein binding to CHEK1, which depends on phosphorylation by ATR[50], and the increase in binding to chromatin and associated proteins, as CHEK1 dissociation from these depends on S296 autophosphorylation[59].

Whereas the functional relevance of most of the observed interactors has been studied, the role of the CHEK1-CLPB interaction change remains unknown. Several studies using different approaches have identified CLPB as an interaction partner of CHEK1[12,60,61] (Fig. 5a), which strongly suggests the formation of mitochondrial CHEK1 complexes of yet unknown function. We were therefore prompted to study the rabusertib-induced CHEK1-CLPB dissociation in more detail. To test whether the dissociation depends on the catalytic activity of CHEK1, we compared dissociation in WT CHEK1, the catalytically inactive D130A mutant and the constitutively active L449R mutant, which is in an open conformation that is constitutively phosphorylated by ATR[35,62]. Rabusertib treatment significantly decreased CLPB in both WT and D130A CHEK1 complexes, whereas CHEK1 L449R-CLPB binding was not affected (Fig. 5b, Supplementary Fig. 7a, b). This suggests that the interaction with CLPB does not depend on catalytic inhibition of CHEK1.

Given that genetic deletion of CLPB results in mitochondrial fragmentation[63] we next analyzed mitochondrial morphology in fixed HeLa cells in the presence or absence of rabusertib using super-resolution microscopy (Fig. 5c). We quantified mitochondria in fragmented and elongated states and identified mitochondrial areas consistent with previous analyses of human mitochondria[64,65] (Supplementary Fig. 7c). Rabusertib treatment caused a significant increase in mitochondrial

fragmentation ($p = 4.3 \times 10^{-3}$, ANOVA followed by Tukey HSD). CHEK1 inactivation can lead to premature and sustained CDK1 activation[66], which in principle could also induce mitochondrial fragmentation via phosphorylation of the GTPase Dynamin-1-like protein (DRP1) controlling mitochondrial fission[67]. To exclude such a mechanism, we analyzed the mitochondrial network in response to rabusertib in combination with the CDK1 inhibitor RO-3306. We confirmed the significant increase in mitochondrial fragmentation even when CDK1 is inhibited by RO-3306 ($p = 1.4 \times 10^{-6}$, ANOVA followed by Tukey HSD), which excludes mitochondrial fragmentation via activation of the CDK1-DRP1 axis.

We had noticed that CHEK1 inhibition by rabusertib can cause DNA damage similar to etoposide treatment as measured by increased histone H2AX phosphorylation (Supplementary Fig. 5h, 6). We therefore asked if mitochondrial fragmentation could also be detected upon etoposide mediated DNA damage. We observed a slight but non-significant increase in mitochondrial fragmentation upon etoposide treatment ($p = 0.151$, two-sided t-test; Supplementary Fig. 7d). This indicates that DNA damage alone cannot explain mitochondrial fragmentation by rabusertib, suggesting the involvement of an additional mechanism. In this regard, rabusertib-induced dissociation of mitochondrial CLPB-CHEK1 complexes represents an intriguing mechanism, though further testing is needed before a causal relationship can be established.

Taken together, we observed that CHEK1 inhibition is associated with changes in PPIs, including dissociation of the known mitochondrial interactor CLPB. We showed that the interaction between CHEK1 and CLPB does not depend on catalytic activity of CHEK1. Based on this finding, we investigated mitochondrial phenotypes upon CHEK1 inhibition. We found that rabusertib induced a significant increase in mitochondrial fragmentation upon CHEK1 inhibition by a mechanism that is independent of CDK1 activation or induction of DNA damage. This illustrates how our multimodal proteomics workflow can be used to identify novel phenotypes associated with probe treatment.

Inhibitor binding induces relocalization of PRKCA to cellular junctions

We found that upon Gö 6983 treatment, PRKCA undergoes structural rearrangements in the KD and AID, but also in other domains, such as the membrane-associating C2 domain. We aimed to profile related interactome changes of PRKCA using AP-MS. Following purification from native lysates obtained from treated cells, we surprisingly noticed a four-fold decrease in PRKCA abundance upon Gö 6983 treatment (Supplementary Fig. 8a, b), limiting the sensitivity of the AP-MS approach. In contrast, we observed no such decrease in PRKCA abundance in the *in vivo* proximity labeling experiment, which applies harsh denaturing lysis conditions, suggesting that Gö 6983 treatment results in PRKCA relocalization to a cell compartment that is insoluble under native lysis conditions.

To characterize the relocalization of inhibitor-bound PRKCA, we focused our analysis on *in vivo* proximity labeling. This approach clearly demonstrated a Gö 6983 induced shift in PRKCA proximity towards membrane associated proteins linked to cell adhesion and cellular junctions (Fig. 6a-c, Supplementary Fig. 8c, d). This included the focal adhesion protein and known PRKCA interactor Integrin beta-1 (ITGB1)[68], but also proteins from tight junctions (OCLN, MARVELD2, CXADR, FMN2, EPB41L4B), adherens junctions (NECTIN2, SNAP23), desmosomes (DSG2) and other junction proteins (ADM4, KIRREL1, MPZL1, TENM3), suggesting that PRKCA relocalizes to very specific membrane structures that control cell-cell contacts and intercellular signaling upon Gö 6983 binding.

Under physiological conditions, the affinity of PRKCA for membrane lipids is regulated by Ca^{2+} binding[69]. We therefore asked if the observed relocalization to membrane structures could be explained via changes in intracellular Ca^{2+} concentrations induced by Gö 6983. We however did not observe any changes in cellular Ca^{2+} concentration upon Gö 6983 treatment using a Fluo-4 calcium imaging assay (Supplementary Fig. 8e). We therefore exclude the possibility that Gö 6983 alters the biochemical context of PRKCA via changes in Ca^{2+} concentration, and propose a model where Gö 6983 binding to PRKCA directly affects the affinity of the kinase for membranes or membrane proteins.

To explore whether catalytic activity is needed for the observed proximity changes, we compared Gö 6983-induced proximity patterns between WT PRKCA, the catalytically inactive PRKCA D463A mutant

and the constitutively active R22A/A25E double mutant[70]. When inhibited, we found similar changes in the proximity of PRKCA WT and both mutants towards the cellular junction proteins (Fig. 6d, cluster 1, Supplementary Fig. 8f, g). Other proximity changes were affected in the mutants compared to the WT (Fig. 6d, cluster 2 and 3), suggesting that these changes may depend on the catalytic activity or the conformation of the AID.

We next wanted to compare our biochemical findings to subcellular localization patterns using live-cell imaging of cells expressing EGFP-PRKCA. Indeed, consistent with our proximity data, we observed Gö 6983-induced relocalization of PRKCA towards the cell periphery, especially at cell-cell contact sites, within 8 minutes (Fig. 6e). In addition to the increased interaction with the plasma membrane, we also noticed a localization towards unknown cytoplasmic foci. Since we saw no enrichment for proteins associated with intracellular organelles, these foci might represent PRKCA aggregates or endosomes containing cell-junction proteins[71].

In summary, we observed that Gö 6983 caused a rapid relocalization of PRKCA towards the plasma membrane, specifically towards complexes involved in cell adhesion and cellular junctions. These changes were observed also in the catalytically inactive and constitutively active mutants upon Gö 6983 treatment, suggesting that these changes are not related to the inhibition of PRKCA kinase activity. PRKCA is known to associate with the plasma membrane through direct contact with lipids upon activation via its C2 domain[72]. Since our AP-LiP-MS data suggest that Gö 6983 binding can trigger structural changes in the C2 domain, we propose that these structural changes expose the C2 domain for subsequent recruitment of PRKCA to specific membrane structures.

In our study on probe binding to CAMKK2, CHEK1, and PRKCA, we applied structural and contextual proteomic methods to characterize overlooked mechanisms of action. We consistently saw structural rearrangements in regulatory domains that at least in part can explain the observed changes in target protein interactions. We have further demonstrated that we can identify additional inhibitory mechanisms of ATP-competitive inhibitors, such as complex stabilization and sequestration of substrates away from other proteins and pathways, predict new phenotypic changes like mitochondrial

fragmentation, and characterize probe-induced protein functions like membrane association. These examples demonstrate how proteomics can be leveraged to investigate small molecule protein binders.

Discussion

ATP competitive kinase inhibitors are primarily designed to block the catalytic activity of their target, but their effect on other critical kinase functions is largely unknown. We introduced a multimodal proteomics strategy to characterize changes in the conformational and interaction landscapes of kinases upon inhibitor binding. Such non-canonical mechanisms may control vital kinase functions such as upstream signal integration and kinase localization, revealing a critical, non-catalytic layer of inhibitor pharmacology.

AP-LiP-MS revealed structural changes distal from the orthosteric binding sites for all four kinases analyzed, suggesting that allosteric structural changes indeed are more frequently linked to inhibitor binding than previously anticipated. These changes are best explained by dissociation of DDIs between the AID and the KD. As accessibility of the ATP-binding pocket is a prerequisite for binding ATP-competitive inhibitors, and AIDs often block access to this site, we reasoned that these inhibitors can only bind and stabilize an open conformation. It remains unclear whether the probe-bound and active conformations are identical. However, the observation that the probe-bound conformation correlates with the formation of complexes typically associated with kinase activation for CAMKK2, CHEK1 and PRKCA suggests that the conformations are similar.

Besides the AID, inhibitor modulated DDIs can also involve other regulatory domains. In the case of PRKCA, AP-LiP-MS data indicated that inhibitor binding may expose the C2 domain, a domain needed for membrane recruitment following PRKCA activation[69]. The second step of our multimodal analysis indeed showed that inhibitor binding strongly induced the proximity of PRKCA to specific membrane proteins at cellular junctions, which we could validate using live-cell imaging. As also shown for the other inhibitors in this study, structural and subsequent contextual proteomics provides critical molecular details on how these compounds reshape the biochemical environment of their target,

thereby generating the necessary information for functional hypothesis testing. Specifically, CAMKK2 inhibitor SGC-CAMKK2-1 induced stable complex formation with PRKAA1 blocking its activation by upstream kinases, such as LKB1. This example showed how a specific CAMKK2 inhibitor can attenuate activity of a non-target kinase via scaffolding. Likewise, CHEK1 inhibitor rabusertib disrupted complex formation with CLBP, a protein controlling mitochondrial homeostasis and stress responses. Intriguingly, the same inhibitor also induced mitochondrial fragmentation. Together these findings suggest a promising new avenue to disentangle a potential role of CHEK1 in coordinating the DNA-damage response with mitochondrial stress response pathways. These examples demonstrate how structural and contextual proteomics go hand in hand to efficiently identify novel inhibitor-induced allosteric gain of function mechanisms.

Together with previous reports, it emerges that the ATP-binding site is a major organizing center of kinase conformation. X-ray crystallography studies revealed that type I and II inhibitors can stabilize either an active DFG-in or inactive DFG-out conformation of the KD, respectively[73]. The DFG-in and DFG-out classification, although initially useful, turned out to be insufficient to fully explain drug action and cellular phenotypes. Besides the KD, kinases consist of multiple other domains and unstructured regions, both of which typically are not resolved in X-ray structures. Alternative methods, including HDX-MS, NMR spectroscopy and FRET have been used to investigate changes in structure beyond the KD. For example, HDX-MS revealed the disruption of the interaction between the pleckstrin homology domain (PHD) and the KD of AKT1 following A-443654 binding resulting in a transition from a PHD-locked-in to a PHD-out conformation[8]. This facilitates membrane binding of AKT1. Given the conserved nature of the KD it is conceivable that a large fraction of kinases will undergo similar allosteric changes in response to ATP-competitive inhibitors. Beyond AKT1, however, only a handful of such allosteric changes have been reported so far, including in BRAF[6], ABL1[9] and the MAPKs p38α and Erk2[74].

The limited number of currently reported allosteric inhibitor responses reflects the inherently low throughput of current structural methods. Multimodal proteomic target engagement analyses as presented here could help address this limitation by enabling high throughput detection and

characterization of allosteric effects induced by ATP-competitive inhibitors across the kinase family. This could provide the scalability needed to systematically explore the growing diversity of high-quality inhibitors and their target interactions, allowing the aggregation of dynamic data that could be used to model effects of small molecule-protein interactions.

Most kinases consist of multiple domains mediating critical non-catalytic kinase functions[75] which in principle could be modulated by ATP-competitive inhibitors in many more kinases than currently known. Besides protein-protein interactions, multiple other non-catalytic kinase functions are known, including non-kinase catalytic activities or regulation of transcription[76]. Based on this, we recommend that ATP-competitive inhibitors, and small molecule protein binders in general, should be carefully characterized during development for possible modulation of non-catalytic protein functions. This might lead to the early discovery of off-mechanism effects that can either be avoided or exploited for drug repurposing.

In addition to characterizing off-mechanism effects of ATP-competitive inhibitors, our approach could facilitate the development of new classes of inhibitors that modulate specific non-catalytic functions, a small but promising group of compounds[77]. This in turn may facilitate the targeting of additional classes of proteins with no known catalytic activity, for example pseudokinases[78,79]. Thus, our workflow could aid in expanding both compound classes and their target landscape.

While our workflow enables the systematic characterization of allosteric non-catalytic modes of action based on changes on protein structure and PPIs, several limitations remain. Our workflow cannot capture effects on additional catalytic activities. Specific targeted assays would need to be combined with our method to cover these. Additionally, some targets and their interactors may not be expressed in HEK293 cells and therefore require multimodal proteomics to be adapted and performed in a different cellular model using viral expression systems or CRISPR mediated tagging of target genes.

We envision that the proteomic characterization of structural and contextual changes will be used during compound development alongside established assays to understand how a compound modulates non-catalytic protein functions. This enables prediction of additional molecular and

phenotypic changes, exploitation of additional modes of action of a compound, and development of drugs that combine or isolate specific modes of action. Our workflow therefore provides valuable information towards the development of safe and effective therapeutics.

Methods

Generation of expression constructs

We generated doxycycline-inducible expression vectors of N-terminal Strep-HA-tagged, miniTurboID-tagged or EGFP-tagged bait proteins using the destination vectors pcDNA5-FRT-TO-SH-GW[80], pcDNA5-pDEST-FRT-MiniTurboID-Flag-N-term, or pcDNA5-pDEST-FRT-EGFP-Flag-N-term, respectively. Human ORFs were provided as pDONR223 vectors selected from addgene, Gateway compatible human orfeome collections horfeome v5.1, horfeome v8.1 and ORFeome Collaboration Clones[81] (OpenBiosystems, Horizon Discovery) or from a kinome orf collection[82] (Supplementary Table 3). Mutations were introduced using a QuickChange II Site-Directed Mutagenesis Kit (Agilent) with primers listed in Supplementary Table 4. The LR reaction was done as described previously[83]. In brief, 150 ng of the destination vector and 300ng of the pDONR223 vector were mixed and diluted with TE buffer (pH 8.0) to a total volume of 4 µL. LR reaction was performed with 1 µL of LR Clonase II enzyme mix (Thermo Fisher Scientific) at 25°C for 1 h and transformed into OmniMAX competent *E. coli* cells (Thermo Fisher Scientific). The transformation mixture was plated onto LB plates containing 100 µg/ml ampicillin and incubated at 37°C o/n and plasmid DNA was isolated from individual colonies by using a QIAprep Spin Miniprep kit (Qiagen) according to the manufacturer's instructions and confirmed by sequencing.

Generation of stable inducible cell lines

The stable inducible cell lines were generated as described previously[83] with the following alterations: 3 x 10^5 T-Rex-HEK293 Flp-In cells (R78007, Invitrogen) were seeded onto six-well plates in DMEM supplemented with 10% fetal bovine serum (FBS) and 1% penicillin-streptomycin (P/S) and incubated

at 37°C and 5% CO_2 o/n. The cells were transfected with the following mixture: 100 ng of the respective expression vector, 900 ng of pOG44 (Invitrogen), 5.7 µl x-tremeGENE 9 DNA transfection reagent (Roche) and 94.3 µl DMEM. The mixture was incubated for 15 minutes at room temperature and added to the cells. The next day, new DMEM supplemented with 10% fetal bovine serum (FBS) and 1% penicillin-streptomycin (P/S) was added. The following day the cells were split into a T150 flask with a total volume of 32 ml. The next day hygromycin B was added at a final concentration of 100 µg/ml and hygromycin resistant recombinant cell pools were selected. Each new cell line was mycoplasma tested before use in experiments.

Cultivation of cells for AP-LiP-MS and AP-MS experiments

HEK293 cells inducibly expressing the strep-HA-tagged bait proteins or EGFP (for AP-MS only) were seeded at a density of 10^7 in 25 ml DMEM supplemented with 10% FCS (BioConcept) and 1% P/S in a 15 cm dish. The cells were incubated at 37°C and 5% CO_2 o/n. Protein expression was induced with 1.3 µg/ml doxycycline for 24 hours before treatment with 1 µM inhibitor (DCLK1-IN-1: Med Chem Express; SGC-CAMKK2-1: Sigma; rabusertib: Med Chem Express; Gö 6983: Med Chem Express) or 0.01% DMSO for 4 hours. Per sample, cells from two 15 cm dishes were harvested by scraping in cold PBS. Each sample was washed in PBS and flash frozen in liquid nitrogen.

Cultivation of cells for proximity labeling experiments

HEK293 cells inducibly expressing the miniTurbo-tagged bait proteins or EGFP were seeded at a density of 10^7 in 25 ml DMEM supplemented with 10% dialyzed FCS (BioConcept) and 1% P/S in a 15 cm dish. The cells were incubated at 37°C and 5% CO_2 o/n. Protein expression was induced with 1.3 µg/ml doxycycline for 24 hours before they were treated with 1 µM inhibitor or 0.01% DMSO for 4 hours. An hour before harvesting, cells were treated with 50 µM biotin. Cells were harvested by dissociation in cold PBS with 1 mM EDTA. Each sample was washed in PBS and flash frozen in liquid nitrogen.

AP-LiP-MS

Pellets were lysed by resolubilizing in 2 ml HNN buffer (50 mM HEPES pH 8.0, 150 mM NaCl, 50 mM NaF) supplemented with 0.5% IGEPAL, 400 nM Na_3VO_4, 1 mM PMSF and 0.2% Protease Inhibitor Cocktail (Sigma). The lysate was incubated on ice for 10 minutes and centrifuged at 18000x g for 20 minutes at 4˚C. The supernatant was added to 80 µl StrepTactin Sepharose slurry (IBA Lifesciences) and incubated on a rotating wheel for 60 minutes at 4˚C. The beads were loaded onto a 1 µm glass filter column and washed 3 times with 1 ml HNN buffer supplemented with 0.5% IGEPAL and 400 nM Na_3VO_4, 3 times with 1 ml HNN buffer, and 3 times with LiP buffer (1 mM $MgCl_2$, 150 mM KCl and 100 mM HEPES pH 7.5). Samples were eluted twice by incubation with 30 µl of 0.5 mM biotin in LiP buffer for 15 minutes. The eluate was pooled and the total protein concentration was determined using a BCA protein assay kit (Pierce) according to the manufacturer's protocol. Measured protein concentrations were between 0.06 µg/µl and 0.1 µg/µl. For each sample, 50 µl eluate was used. Samples were then processed as previously described[84]. Briefly, samples were treated with 10 µM inhibitor or 2% DMSO in triplicates and incubated at 25˚C for 5 minutes. Proteinase K (Sigma) at an enzyme:substrate ratio of 1:100 was added for 5 minutes. Proteolysis was stopped by incubation at 99˚C for 5 minutes. Samples were then diluted with 10% sodium deoxycholate (DOC) for a final concentration of 5% DOC. Samples were reduced with 5 mM TCEP for 40 minutes at 37°C and 200 rpm, and alkylated with 40 mM IAA for 30 minutes at 30°C in the dark, at 200 rpm. Samples were diluted with 100 mM ammonium bicarbonate to a DOC concentration of 1%. To each sample, 1 µg Lys-C and 1 µg trypsin was added and samples were incubated o/n at 37°C and 200 rpm. The digestion was stopped with 2% formic acid (FA) and precipitated DOC was removed by filtration using 0.2 µm PVDF filters.

AP-MS

Cell pellets were lysed by resolubilizing in 2 ml HNN buffer supplemented with 0.5% IGEPAL or 1% DDM when using PRKCA as bait, 400 nM Na_3VO_4, 1 mM PMSF, 0.2% Protease Inhibitor Cocktail (Sigma) and

0.5 µl/ml benzonase (Sigma). The lysate was incubated on ice for 10 minutes and centrifuged at 18000x g for 20 minutes at 4˚C. The pulldown was done as for AP-LiP-MS samples, except that the final wash was done with 100 mM ammonium bicarbonate. Samples were eluted twice by incubation with 30 µl of 0.5 mM biotin in 100 mM ammonium bicarbonate for 15 minutes. To the samples, 60 µl 8 M urea in 100 mM ammonium bicarbonate for a final concentration of 4 M urea. Samples were reduced and alkylated as for AP-LiP-MS. Samples were diluted with 100 mM ammonium bicarbonate to a urea concentration of 1 M. To each sample, 1 µg Lys-C and 1 µg trypsin was added and samples were incubated o/n at 37°C and 200 rpm. The digestion was stopped with 2% FA.

In vivo proximity labeling

Cell pellets were lysed in 1 ml RIPA buffer (50 mM Tris-HCl pH 8, 150 mM NaCl, 1 % Triton, 1mM EDTA, 0.1 % SDS) supplemented with 1 mM PMSF, 0.2% Protease Inhibitor Cocktail (Sigma) and 0.5 µl/ml benzonase (Sigma). The lysate was briefly sonicated for 30 s, incubated at 10˚C for 30 minutes and centrifuged at 18000x g for 20 minutes at 4˚C. The supernatant was added to protease resistant 120 µl StrepTactin Sepharose slurry (IBA Lifesciences) that were modified as previously described[85] and incubated on a rotating wheel for 60 minutes at 4˚C. The beads were loaded onto a 1 µm glass filter plate and washed 3 times with 1 ml RIPA buffer, 3 times with 1 ml HNN buffer, 3 times with 100 mM ammonium bicarbonate and transferred to a 10 kDa cutoff plate and centrifuged at 1500x g for 15 minutes. To the samples, 100 µl of 8 M urea was added. Samples were reduced with 10 mM TCEP for 30 minutes at 37 °C and 200 rpm, and alkylated with 40 mM IAA for 30 minutes at 37°C in the dark, at 200 rpm. Following centrifugation at 1500x g for 15 minutes, beads were washed twice with 250 µl of 100 mM ammonium bicarbonate and resuspended in 200 µl of 100 mM ammonium bicarbonate. Samples were digested o/n at 37°C at 200 rpm in the presence of 1 µg trypsin and 1 µg Lys-C. Peptides were collected by centrifugation at 1500x g for 20 minutes from the supernatant and combined with the peptides from the supernatant obtained from washing the digested beads with 100 µl of 100 mM ammonium bicarbonate and centrifugation at 1500x g for 40 minutes. The digestion was stopped with 5% FA.

Desalting

Samples were desalted using HNFR S18V desalting plates (Nest Group). The resin was activated using 200 µl methanol and washed 3 times with 200 µl Buffer B (50% ACN and 0.1% FA for AP-LiP and AP samples, 40% ACN and 0.1% FA for proximity labeling samples). The resin was equilibrated 3 times with 200 µl Buffer A (0.1% FA for AP-LiP and AP samples, 5% ACN and 0.1% FA for proximity labeling samples). Samples were loaded and washed 3 times with 200 µl Buffer A. Samples were eluted twice with 100 µl Buffer B and dried in a vacuum centrifuge.

Mass spectrometry

AP-LiP-MS, AP-MS and PRKCA proximity labeling experiments were measured on a Orbitrap Fusion Lumos Tribrid mass spectrometer (Thermo Fisher Scientific) equipped with an Acquity M-Class UPLC System (Waters). To separate the peptides on self-pack 40 cm x 0.75 µm fritted emitter (CoAnn) packed with 3 µm C18 beads (Dr. Maisch), we used a linear gradient of 3% to 35% acetonitrile in water with 0.1% FA over the course of 120 minutes at flow rate of 300 nl/min. Library samples consisting of pools of replicates were measured by DDA. The MS1 spectra were acquired in a scan range of 350-1150m/z with an Orbitrap resolution of 120000. The normalized automatic gain control (AGC) target was set to 200% with a maximum injection time of 100 ms. The RF lens was set to 30%. The targeted MS2 spectra were acquired for the top 20 peaks in the spectrum and fragmented with a HCD of 30%. The spectra were measured with an Orbitrap resolution of 30000 with isolation windows of 1.6 m/z. The AGC target was set to 200% with a maximum injection time of 54 ms. Samples for quantification were measured by DIA. The MS1 spectra were acquired in a scan range of 350-1400 m/z with an Orbitrap resolution of 120000. The normalized AGC target was set to 50% with a maximum injection time of 100 ms. The RF lens was set to 30%. The targeted MS2 spectra were acquired for the desired masses with variable isolation windows (Supplementary Table 5) and fragmented with a HCD of 28%. The spectra were measured with an Orbitrap resolution of 30000 with variable scan ranges. The AGC target was set to 200% with a maximum injection time of 54 ms. The RF lens was set to 30%.

Proximity labeling samples were measured on an Orbitrap Exploris 480 mass spectrometer (Thermo Fischer Scientific) equipped with an EASY-nLC 1000 System (Thermo Fischer Scientific). Peptides were separated on the same column used for the Orbitrap Fusion Lumos Tribrid mass spectrometer using a linear gradient of 5% to 30% acetonitrile in water (0.1% FA) over the course of 120 minutes at flow rate of 300 nl/min. Library samples consisting of pools of replicates were measured by DDA. The MS spectra were acquired at an Orbitrap resolution of 120000 between 350 m/z and 1500 m/z. The normalized AGC target was set to 200% or a maximum injection time of 100 ms. Subsequently, 20 MS/MS spectra were acquired after higher-energy collisional dissociation (HCD) with a normalized collision energy of 30%, an Orbitrap resolution of 30000, and a normalized AGC target of 200% or a maximum injection time of 54 ms. Precursors with a minimum intensity of 5000 ion counts and a charge state between 2 and 6 were selected with a mass window of 1.4 m/z. A dynamic exclusion window of 20 s was used.

Samples for quantification were measured by DIA. The MS1 spectra were acquired in a scan range of 350-1150m/z with an Orbitrap resolution of 120000. The normalized AGC target was set to 200% with a maximum injection time of 264 ms. The RF lens was set to 50%. The targeted MS2 spectra were acquired for the desired masses with variable isolation windows (Supplementary Table 6) and fragmented with a HCD of 30%. The spectra are measured with an Orbitrap resolution of 30000 with variable scan ranges. The AGC target was set to 200% with a maximum injection time of 66 ms. The RF lens was set to 50%.

Search of Mass Spectrometry data

Spectra were searched using Spectronaut v. 19 in directDIA mode with the measured DDA library files used to extend the library. Searches were done separately for each experiment and bait. For AP-LiP-MS and AP-MS data, semi-specific peptides were included in the search, and phosphorylation was included as a variable modification. For proximity labeling data, only specific peptides were included in the search, and the number of missed cleavages allowed was four. Both biotinylation and phosphorylation were included as variable modifications. For all searches, cross-run normalization was

turned off. Report files were exported and imported into R version 4 and analyzed using protti version 0.6.0[86].

Determination of structural changes in AP-LiP-MS data

The code for all analyses is available on github.com/vivreb/multi-proteomic_profiling_of_kinases/. Identified peaks were filtered for q-value < 0.001, $\log_2$(intensity) > 10 and Δrt < 0.1 minutes, where Δrt was defined as the difference between the predicted retention time and the empirical apex retention time. Peptides were filtered for proteotypicity and common contaminants were removed. Only peptides that were complete across all conditions were used for further analysis. Peptide abundance was normalized based on rank invariant values using the MBQN package[87]. Differential abundance was calculated using a moderated t-test[88]. Multiple testing correction was performed using the Benjamini-Hochberg procedure[89]. Peptides with an absolute $\log_2$(fold change) > 0.585 (corresponding to a fold change > 1.5) and adjusted p-value < 0.05 were considered significantly changing.

Determination of interactors in AP-MS data

Identified peaks were filtered for q-value < 0.001, $\log_2$(intensity) > 9 and Δrt < 1 minute. Peptides were filtered for specificity and proteotypicity. Only peptides that were found in all replicates within a given condition were used for further analysis. Peptide abundance was normalized based on rank invariant values using the MBQN package[87] and bait normalized. Protein abundance was calculated by MaxLFQ[90] for proteins with at least 3 peptides. We used a modified version of the weighted D-score[91] to determine interactors. First, we used protein intensity instead of spectral count, and we augmented the D-score 1.1-fold for known interactors based on physical interactions in the BioGrid database[40]. We consider proteins that have a modified D-score > 1.425 as interactors (Supplementary Fig. 9a). We confirmed that we effectively recover known interactors using a ROC area under the curve (AUC) analysis (AUC = 0.992, Supplementary Fig. 9b).

Determination of interaction changes in AP-MS data

Peptides were filtered and normalized as for the determination of interactors before imputation using msImpute[92] and protein abundance calculation using MaxLFQ[90]. For all interactors, the differential abundance was calculated using a moderated t-test[88]. Multiple testing correction was performed using the Benjamini-Hochberg procedure[89]. Proteins with an absolute $\log_2$(fold change) > 1 and adjusted p-value < 0.05 were considered significantly changing.

Determination of phosphorylation changes in AP-MS data

Filtering was done as for the AP-LiP-MS analysis. Peptide abundance was normalized based on rank invariant values using the MBQN package[87] and bait normalized. Only peptides complete in at least one condition were kept for further analysis, and peptides were imputed using msImpute[92]. Only peptides containing a phosphorylation were considered for the analysis. Differential abundance was calculated using a moderated t-test[88]. Multiple testing correction was performed using the Benjamini-Hochberg procedure[89]. Peptides with an absolute $\log_2$(fold change) > 0.585 (corresponding to a fold change > 1.5) and adjusted p-value < 0.05 were considered significantly changing.

Determination of proximity changes in proximity labeling data

Identified peaks were filtered for q-value < 0.0001, $\log_2$(intensity) > 9 and Δrt < 0.5 minutes. Peptides were filtered for proteotypicity and common contaminants were removed. Peptide abundance was normalized based on rank invariant values using the MBQN package[87]. Protein abundance was calculated by MaxLFQ[90] for proteins with at least 3 peptides. Differential abundance was calculated using a moderated t-test[88]. Multiple testing correction was performed using the Benjamini-Hochberg procedure[89]. The same calculations were performed for an EGFP control, and proteins showing a change in the same direction as in the control were removed from the data. Adjusted p-values were recalculated for the revised dataset. Proteins with an absolute $\log_2$(fold change) > 1 and adjusted p-value < 0.05 were considered significantly changing.

siRNA-mediated knockdown

HEK293 cells (ATCC) were seeded at 10^5 cells per well in a 6-well plate in DMEM supplemented with 10% dialyzed FBS (BioConcept). To each well, 50 µM siRNA (siCAMKK2: s20926, Thermo Fisher Scientific; siNEG: iSilencer/i Negative Control No. 1, Thermo Fisher Scientific) and 7 µl siPORT NeoFX transfection reagent (Thermo Fisher Scientific) was added. Cells were grown for 72 h. Samples were treated with 10 µM SGC-CAMKK2-1 for 4 h in 0.01% DMSO and glucose starved for 20 min in glucose-free DMEM (Gibco) supplemented with 10% dialyzed FBS (BioConcept) before harvesting. Samples were harvested in 100 µl RIPA buffer supplemented with PI, PMSF, Na3VO4 and 0.5µg/ml benzonase and snap frozen. Samples were stored at -80˚C until processing.

Western blot analysis

Samples were thawed on ice, and centrifuged at 18000x g for 20 minutes and the supernatant was collected. Total protein concentration was measured using a BCA assay (Pierce), and the samples were diluted to 2.5 µg/µl. The samples were mixed with 4x Lämmli buffer (Invitrogen) and heated to 95°C for 5 minutes. Of the samples, 20 µl were loaded onto pre-cast 4-12% Bis-Tris gels (Invitrogen) along with 5 µl of the ladder (BioRad). The gel was run at 100 V for 60 minutes. The gel was blotted onto a nitrocellulose membrane (BioRad) for 30 minutes. The membrane was blocked with 5% milk in TBST (20 mM Tris pH 7.6, 150 mM NaCl, 1% TWEEN 20) for 1 h. The primary antibody (anti-pT183 PRKAA1: Cell Signaling Technology (D4D6D); anti-PRKAA1: Cell Signaling Technology (2532); anti-CAMKK2: Proteintech (11549-1-AP); anti-γH2AX: Merck (05-636); anti-H2AX: Sigma (PLA0023); anti-GAPDH: Invitrogen (GA1R)) was added for 2 h at room temperature or o/n at 4˚C and subsequently washed for 3x 10 minutes with TBST. The secondary antibody (anti-mouse secondary antibody: Cell Signaling Technology (7076S), anti-rabbit secondary antibody: Cell Signaling Technology (7074S); all diluted 1:1000) was added for 1 hour at RT. The membrane was again washed for 3x 10 minutes. The ECL detection reagent (Cytiva) was added and the membrane was imaged by chemiluminescence with

various exposure times. The antibodies were removed by incubation in western blot stripping buffer (Invitrogen) for 10 min, washed in TBST and blocked before the next antibody was added.

AlphaFold3 Prediction and Structural Analysis

The AlphaFold3[48] prediction of the CAMKK2-PRKAA1 complex was generated using the AlphaFold3 webserver (alphafoldserver.com/). Only the sequences of the KDs were used (Supplementary Table 7). The interface analysis was done in the PyMOL Molecular Graphics System version 2.5.3. The interface comprises residues that are within 2.8 Å of the other protein and show a change in accessible surface area (ΔASA) of at least 1 $Å^2$ upon binding the interaction partner.

Live cell imaging

HEK293 cells expressing N-terminally tagged EGFP-PRKCA were seeded at 10^5 cells in 35 mm glass-bottom cell culture dishes (Ibidi) in DMEM supplemented with 10% dialyzed FBS (BioConcept) and 1% P/S, and induced for 24 h with 1.3 µg/ml doxycycline. For imaging, FluoroBrite DMEM (Gibco) supplemented with 10% dialyzed FBS (BioConcept), 1% P/S and 1.3 µg/ml doxycycline was used. To the cells, 1 µM Gö 6983 in 0.01% DMSO diluted in 100 µl imaging medium was added and cells were immediately imaged using an instant Structured Illumination Microscope (VisiTech). Z-stacks were acquired across 5 time points 2 minutes apart. Images were deconvolved using Huygens Professional 24.10. Individual slices from representative cells were normalized and cropped using ImageJ and a scale bar showing 5 µm was added.

Immunofluorescence microscopy

HeLa CCL2 cells (ATCC) were seeded at 10^5 cells per well in a 6-well plate containing cover slips in DMEM supplemented with 10% dialyzed FBS (BioConcept) and 1% P/S and grown o/n. To the cells, 1 µM rabusertib for 4 h, 6 µM RO-3306 (Sigma) for 24 h, or 50 µM etoposide (Sigma) for 3 h was added in 0.01% DMSO. The cells were incubated with 100 nM MitoTracker Deep Red FM (Invitrogen) for 1 h. Cells were subsequently washed with warm PBS and fixed with 4% PFA in PBS (Invitrogen) for 15

minutes. Cells were washed and the coverslips mounted on slides using ProLong Diamond mounting medium (Invitrogen). Z-stacks of the samples were imaged using an instant Structured Illumination Microscope (VisiTech). Images were deconvolved using Huygens Professional 24.10 and cropped using ImageJ. Image segmentation was performed in Ilastik 1[93]. The number of pixels from fragmented mitochondria were counted and normalized based on the total number of pixels from mitochondria in each image. Significance was calculated per experiment. To assess significance of rabusertib treatment with and without RO-3306 treatment, we used two-way analysis of variance (ANOVA) followed by a Tukey Honestly Significant Difference (HSD) test. To separately test the effects of etoposide treatment, we used a two-tailed t-test. 10 images taken from 3 replicates were quantified for each condition.

Fluo-4 calcium imaging

HEK293 cells ectopically expressing miniTurbo-PKCa were grown in DMEM supplemented with 10% dialyzed FBS (BioConcept) and 1% P/S, induced with 1.3 µg/ml doxycycline and treated with 1 µM Gö 6983 or 0.01% DMSO for 4 h. Fluo-4 solution was prepared according to manufacturer's instructions (Invitrogen). Baseline fluorescence was measured with an excitation wavelength of 483 nM and an emission wavelength of 530 nM every 58 seconds for 10 cycles. To the samples, 10 µM ionomycin or 1% ethanol, or 1 µM Gö 6983 or 1% DMSO was added. After addition of the reagents, the measurements were repeated for 250 additional cycles. Measurements were normalized to a baseline control without the Fluo-4 reagent and to the respective vehicle control. All measurements were done in six replicates and mean and standard error of the mean were reported.

Acknowledgements

We thank the group of Dr. Anne-Claude Gingras for the pcDNA5-pDEST-FRT-MiniTurboID-Flag vectors. We thank Dr. Natalie de Souza for her comments on the manuscript. We thank ScopeM for their support and assistance with microscopy experiments. This work was supported by the Innovative Medicines Initiative 2 Joint Undertaking (JU) under grant agreement No 875510. The JU receives support from the European Union's Horizon 2020 research and innovation program and EFPIA and

Ontario Institute for Cancer Research, Royal Institution for the Advancement of Learning McGill University, Kungliga Tekniska Hoegskolan, Diamond Light Source Limited.

Data and Code Availability

All MS data and related files are accessible via the ProteomeXchange Consortium via the PRIDE partner repository[94] with the dataset identifier PXD069830. All code and additional data necessary to fully reproduce all analyses is available for download on github via github.com/vivreb/multi-proteomic_profiling_of_kinases/.

References

1. Lahiry, P., Torkamani, A., Schork, N.J. & Hegele, R.A. Kinase mutations in human disease: interpreting genotype-phenotype relationships. *Nat Rev Genet* **11**, 60-74 (2010).
2. Torkamani, A., Verkhivker, G. & Schork, J.N. Cancer driver mutations in protein kinase genes. *Cancer Letters* **281**, 117-127 (2009).
3. Tredup, C. et al. Toward target 2035: EUbOPEN - a public-private partnership to enable & unlock biology in the open. *RSC Med Chem* **16**, 457-464 (2025).
4. Zhang, J., Yang, P.L. & Gray, N.S. Targeting cancer with small molecule kinase inhibitors. *Nat Rev Cancer* **9**, 28-39 (2009).
5. Roskoski, R., Jr. Properties of FDA-approved small molecule protein kinase inhibitors: A 2024 update. *Pharmacol Res* **200**, 107059 (2024).
6. Hatzivassiliou, G. et al. RAF inhibitors prime wild-type RAF to activate the MAPK pathway and enhance growth. *Nature* **464**, 431-5 (2010).
7. Haling, J.R. et al. Structure of the BRAF-MEK complex reveals a kinase activity independent role for BRAF in MAPK signaling. *Cancer Cell* **26**, 402-413 (2014).
8. Shaw, A.L. et al. ATP-competitive and allosteric inhibitors induce differential conformational changes at the autoinhibitory interface of Akt1. *Structure* **31**, 343-354 e3 (2023).
9. Skora, L., Mestan, J., Fabbro, D., Jahnke, W. & Grzesiek, S. NMR reveals the allosteric opening and closing of Abelson tyrosine kinase by ATP-site and myristoyl pocket inhibitors. *Proc Natl Acad Sci USA* **110**, E4437-E4445 (2013).
10. Manning, G., Whyte, D.B., Martinez, R., Hunter, T. & Sudarsanam, S. The protein kinase complement of the human genome. *Science* **298**, 1912-34 (2002).
11. Varjosalo, M. et al. The protein interaction landscape of the human CMGC kinase group. *Cell Rep* **3**, 1306-20 (2013).
12. Buljan, M. et al. Kinase Interaction Network Expands Functional and Disease Roles of Human Kinases. *Mol Cell* **79**, 504-520 e9 (2020).
13. Feng, Y. et al. Global analysis of protein structural changes in complex proteomes. *Nat Biotechnol* **32**, 1036-44 (2014).
14. Roux, K.J., Kim, D.I., Raida, M. & Burke, B. A promiscuous biotin ligase fusion protein identifies proximal and interacting proteins in mammalian cells. *J Cell Biol* **196**, 801-10 (2012).
15. Lambert, J.-P., Tucholska, M., Go, C., Knight, J.D.R. & Gingras, A.-C. Proximity biotinylation and affinity purification are complementary approaches for the interactome mapping of chromatin-associated protein complexes. *J Proteomics* **118**, 81-94 (2015).
16. Nussinov, R. & Tsai, C.J. Allostery in disease and in drug discovery. *Cell* **153**, 293-305 (2013).

17. Li, M., Rehman, U.A., Liu, Y., Chen, K. & Lu, S. Dual roles of ATP-binding site in protein kinases: Orthosteric inhibition and allosteric regulation. in *Adv Protein Chem Struct Biol* Vol. 124 87-119 (2021).
18. Gogl, G., Kornev, A.P., Remenyi, A. & Taylor, S.S. Disordered Protein Kinase Regions in Regulation of Kinase Domain Cores. *Trends Biochem Sci* **44**, 300-311 (2019).
19. Fenton, M., Gregory, E. & Daughdrill, G. Protein disorder and autoinhibition: The role of multivalency and effective concentration. *Curr Opin Struct Biol* **83**, 102705 (2023).
20. Li, M., Cao, H., Lai, L. & Liu, Z. Disordered linkers in multidomain allosteric proteins: Entropic effect to favor the open state or enhanced local concentration to favor the closed state? *Protein Sci* **27**, 1600-1610 (2018).
21. Piazza, I. et al. A machine learning-based chemoproteomic approach to identify drug targets and binding sites in complex proteomes. *Nat Commun* **11**, 4200 (2020).
22. Stalder, P. et al. An approach to characterize mechanisms of action of anti-amyloidogenic compounds in vitro and in situ. *NPJ Parkinsons Dis* **11**, 122 (2025).
23. Holfeld, A. et al. Systematic identification of structure-specific protein-protein interactions. *Mol Syst Biol* **20**, 651-675 (2024).
24. Cheng, L. et al. DCLK1 autoinhibition and activation in tumorigenesis. *Innovation (Camb)* **3**, 100191 (2022).
25. Ferguson, F.M. et al. Discovery of a selective inhibitor of doublecortin like kinase 1. *Nat Chem Biol* **16**, 635-643 (2020).
26. Patel, O. et al. Structural basis for small molecule targeting of Doublecortin Like Kinase 1 with DCLK1-IN-1. *Commun Biol* **4**, 1105 (2021).
27. Kylarova, S., Psenakova, K., Herman, P., Obsilova, V. & Obsil, T. CaMKK2 kinase domain interacts with the autoinhibitory region through the N-terminal lobe including the RP insert. *Biochim Biophys Acta Gen Subj* **1862**, 2304-2313 (2018).
28. Katsuragi, Y. & Sagata, N. Regulation of Chk1 kinase by autoinhibition and ATR-mediated phosphorylation. *Mol Biol Cell* **15**, 1680-9 (2004).
29. House, C. & Kemp, B.E. Protein kinase C contains a pseudosubstrate prototope in its regulatory domain. *Science* **238**, 1726-8 (1987).
30. Sommese, R.F., Ritt, M., Swanson, C.J. & Sivaramakrishnan, S. The Role of Regulatory Domains in Maintaining Autoinhibition in the Multidomain Kinase PKCalpha. *J Biol Chem* **292**, 2873-2880 (2017).
31. Wells, C. et al. SGC-CAMKK2-1: A Chemical Probe for CAMKK2. *Cells* **12**, 287 (2023).
32. King, C. et al. Characterization and preclinical development of LY2603618: a selective and potent Chk1 inhibitor. *Invest New Drugs* **32**, 213-26 (2014).
33. Frings, S. Protein kinase C sensitizes olfactory adenylate cyclase. *J Gen Physiol* **101**, 183-205 (1993).
34. Lippert, L.G. et al. Kinase inhibitors allosterically disrupt a regulatory interaction to enhance PKCalpha membrane translocation. *J Biol Chem* **296**, 100339 (2021).
35. Han, X. et al. Conformational Change of Human Checkpoint Kinase 1 (Chk1) Induced by DNA Damage. *J Biol Chem* **291**, 12951-9 (2016).
36. Orr, J.W. & Newton, A.C. Intrapeptide regulation of protein kinase C. *J Biol Chem* **269**, 8383-7 (1994).
37. Orr, J.W., Keranen, L.M. & Newton, A.C. Reversible exposure of the pseudosubstrate domain of protein kinase C by phosphatidylserine and diacylglycerol. *J Biol Chem* **267**, 15263-6 (1992).
38. Antal, C.E., Violin, J.D., Kunkel, M.T., Skovso, S. & Newton, A.C. Intramolecular conformational changes optimize protein kinase C signaling. *Chem Biol* **21**, 459-469 (2014).
39. Endicott, J.A., Noble, M.E. & Johnson, L.N. The structural basis for control of eukaryotic protein kinases. *Annu Rev Biochem* **81**, 587-613 (2012).

40. Oughtred, R. et al. The BioGRID database: A comprehensive biomedical resource of curated protein, genetic, and chemical interactions. *Protein Sci* **30**, 187-200 (2021).
41. Woods, A. et al. Ca2+/calmodulin-dependent protein kinase kinase-beta acts upstream of AMP-activated protein kinase in mammalian cells. *Cell Metab* **2**, 21-33 (2005).
42. Anderson, K.A. et al. Hypothalamic CaMKK2 contributes to the regulation of energy balance. *Cell Metab* **7**, 377-88 (2008).
43. Green, M.F., Anderson, K.A. & Means, A.R. Characterization of the CaMKKbeta-AMPK signaling complex. *Cell Signal* **23**, 2005-12 (2011).
44. Green, M.F. et al. Ca2+/Calmodulin-dependent protein kinase kinase beta is regulated by multisite phosphorylation. *J Biol Chem* **286**, 28066-79 (2011).
45. Xy Ling, N. et al. Functional analysis of an R311C variant of Ca(2+) -calmodulin-dependent protein kinase kinase-2 (CaMKK2) found as a de novo mutation in a patient with bipolar disorder. *Bipolar Disord* **22**, 841-848 (2020).
46. Tokumitsu, H., Hatano, N., Fujimoto, T., Yurimoto, S. & Kobayashi, R. Generation of autonomous activity of Ca(2+)/calmodulin-dependent protein kinase kinase beta by autophosphorylation. *Biochemistry* **50**, 8193-201 (2011).
47. Ishikawa, Y. et al. Identification and characterization of novel components of a Ca2+/calmodulin-dependent protein kinase cascade in HeLa cells. *FEBS Lett* **550**, 57-63 (2003).
48. Abramson, J. et al. Accurate structure prediction of biomolecular interactions with AlphaFold 3. *Nature* **630**, 493-500 (2024).
49. Shaw, R.J. et al. The kinase LKB1 mediates glucose homeostasis in liver and therapeutic effects of metformin. *Science* **310**, 1642-6 (2005).
50. Jiang, K. et al. Regulation of Chk1 includes chromatin association and 14-3-3 binding following phosphorylation on Ser-345. *J Biol Chem* **278**, 25207-17 (2003).
51. Alonso-de Vega, I., Martin, Y. & Smits, V.A. USP7 controls Chk1 protein stability by direct deubiquitination. *Cell Cycle* **13**, 3921-6 (2014).
52. Zhang, P. et al. ATM-mediated stabilization of ZEB1 promotes DNA damage response and radioresistance through CHK1. *Nat Cell Biol* **16**, 864-75 (2014).
53. Scorah, J. et al. A conserved proliferating cell nuclear antigen-interacting protein sequence in Chk1 is required for checkpoint function. *J Biol Chem* **283**, 17250-9 (2008).
54. Han, X., Aslanian, A., Fu, K., Tsuji, T. & Zhang, Y. The Interaction between Checkpoint Kinase 1 (Chk1) and the Minichromosome Maintenance (MCM) Complex Is Required for DNA Damage-induced Chk1 Phosphorylation. *J Biol Chem* **289**, 24716-24723 (2014).
55. Liu, S. et al. Claspin operates downstream of TopBP1 to direct ATR signaling towards Chk1 activation. *Mol Cell Biol* **26**, 6056-64 (2006).
56. Leung-Pineda, V., Ryan, C.E. & Piwnica-Worms, H. Phosphorylation of Chk1 by ATR is antagonized by a Chk1-regulated protein phosphatase 2A circuit. *Mol Cell Biol* **26**, 7529-38 (2006).
57. Booth, L. et al. PARP and CHK inhibitors interact to cause DNA damage and cell death in mammary carcinoma cells. *Cancer Biol Ther* **14**, 458-65 (2013).
58. Okita, N., Minato, S., Ohmi, E., Tanuma, S. & Higami, Y. DNA damage-induced CHK1 autophosphorylation at Ser296 is regulated by an intramolecular mechanism. *FEBS Lett* **586**, 3974-9 (2012).
59. Kasahara, K. et al. 14-3-3gamma mediates Cdc25A proteolysis to block premature mitotic entry after DNA damage. *EMBO J* **29**, 2802-12 (2010).
60. Antonicka, H. et al. A High-Density Human Mitochondrial Proximity Interaction Network. *Cell Metab* **32**, 479-497 (2020).
61. Golkowski, M. et al. Multiplexed kinase interactome profiling quantifies cellular network activity and plasticity. *Mol Cell* **83**, 803-818 (2023).

62. Wang, J., Han, X. & Zhang, Y. Autoregulatory mechanisms of phosphorylation of checkpoint kinase 1. *Cancer Res* **72**, 3786-94 (2012).
63. D'Angelo, D. et al. Dependence of mitochondrial calcium signalling and dynamics on the disaggregase, CLPB. *Nat Commun* **16**, 2810 (2025).
64. Wiemerslage, L. & Lee, D. Quantification of mitochondrial morphology in neurites of dopaminergic neurons using multiple parameters. *J Neurosc Methods* **262**, 56-65 (2016).
65. Shami, J.G. et al. Three-dimensional ultrastructure of giant mitochondria in human non-alcoholic fatty liver disease. *Sci Rep* **11**(2021).
66. Sanchez, Y. et al. Conservation of the Chk1 Checkpoint Pathway in Mammals: Linkage of DNA Damage to Cdk Regulation Through Cdc25. *Science* **277**, 1497-1501 (1997).
67. Taguchi, N., Ishihara, N., Jofuku, A., Oka, T. & Mihara, K. Mitotic phosphorylation of dynamin-related GTPase Drp1 participates in mitochondrial fission. *J Biol Chem* **282**, 11521-9 (2007).
68. Ng, T. et al. PKCalpha regulates beta1 integrin-dependent cell motility through association and control of integrin traffic. *EMBO J* **18**, 3909-23 (1999).
69. Medkova, M. & Cho, W. Mutagenesis of the C2 domain of protein kinase C-alpha. Differential roles of Ca2+ ligands and membrane binding residues. *J Biol Chem* **273**, 17544-52 (1998).
70. Ueda, Y. et al. Protein kinase C activates the MEK-ERK pathway in a manner independent of Ras and dependent on Raf. *J Biol Chem* **271**, 23512-9 (1996).
71. Stamatovic, S.M., Johnson, A.M., Sladojevic, N., Keep, R.F. & Andjelkovic, A.V. Endocytosis of tight junction proteins and the regulation of degradation and recycling. *Ann N Y Acad Sci* **1397**, 54-65 (2017).
72. Evans, J.H., Murray, D., Leslie, C.C. & Falke, J.J. Specific translocation of protein kinase Calpha to the plasma membrane requires both Ca2+ and PIP2 recognition by its C2 domain. *Mol Biol Cell* **17**, 56-66 (2006).
73. Nolen, B., Taylor, S. & Ghosh, G. Regulation of protein kinases; controlling activity through activation segment conformation. *Mol Cell* **15**, 661-75 (2004).
74. Hari, S.B., Merritt, E.A. & Maly, D.J. Conformation-Selective ATP-Competitive Inhibitors Control Regulatory Interactions and Noncatalytic Functions of Mitogen-Activated Protein Kinases. *Chem Biol* **21**, 628-635 (2014).
75. Kung, J.E. & Jura, N. Structural Basis for the Non-catalytic Functions of Protein Kinases. *Structure* **24**, 7-24 (2016).
76. Hu, S. et al. Profiling the Human Protein-DNA Interactome Reveals ERK2 as a Transcriptional Repressor of Interferon Signaling. *Cell* **139**, 610-622 (2009).
77. Wang, Z., Huang, W., Zhou, K., Ren, X. & Ding, K. Targeting the Non-Catalytic Functions: a New Paradigm for Kinase Drug Discovery? *J Med Chem* **65**, 1735-1748 (2022).
78. Preuss, F., Chatterjee, D., Dederer, V., Knapp, S. & Mathea, S. Enabling pseudokinases as potential drug targets. in *Methods Enzymol* 663-683 (2022).
79. Reiterer, V., Eyers, P.A. & Farhan, H. Day of the dead: pseudokinases and pseudophosphatases in physiology and disease. *Trends Cell Biol* **24**, 489-505 (2014).
80. Glatter, T., Wepf, A., Aebersold, R. & Gstaiger, M. An integrated workflow for charting the human interaction proteome: insights into the PP2A system. *Mol Syst Biol* **5**, 237 (2009).
81. Collaboration, T.O. The ORFeome Collaboration: a genome-scale human ORF-clone resource. *Nat Methods* **13**, 191-192 (2016).
82. Varjosalo, M. et al. Application of active and kinase-deficient kinome collection for identification of kinases regulating hedgehog signaling. *Cell* **133**, 537-48 (2008).
83. Liu, X., Salokas, K., Weldatsadik, R.G., Gawriyski, L. & Varjosalo, M. Combined proximity labeling and affinity purification-mass spectrometry workflow for mapping and visualizing protein interaction networks. *Nat Protoc* **15**, 3182-3211 (2020).
84. Reber, V. & Gstaiger, M. Target Deconvolution by Limited Proteolysis Coupled to Mass Spectrometry. in *Methods Mol Biol* 177-190 (2023).

85. Rafiee, M.R. et al. Protease-resistant streptavidin for interaction proteomics. *Mol Syst Biol* **16**, e9370 (2020).
86. Quast, J.P., Schuster, D. & Picotti, P. protti: an R package for comprehensive data analysis of peptide- and protein-centric bottom-up proteomics data. *Bioinform Adv* **2**, vbab041 (2022).
87. Brombacher, E., Schad, A. & Kreutz, C. Tail-Robust Quantile Normalization. *Proteomics* **20**, 2000068 (2020).
88. Ritchie, M.E. et al. limma powers differential expression analyses for RNA-sequencing and microarray studies. *Nucleic Acids Res* **43**, e47 (2015).
89. Benjamini, Y. & Hochberg, Y. Controlling the False Discovery Rate - a Practical and Powerful Approach to Multiple Testing. *J R Stat Soc B Stat Methodol* **57**, 289-300 (1995).
90. Cox, J. et al. Accurate proteome-wide label-free quantification by delayed normalization and maximal peptide ratio extraction, termed MaxLFQ. *Mol Cell Proteomics* **13**, 2513-26 (2014).
91. Sowa, M.E., Bennett, E.J., Gygi, S.P. & Harper, J.W. Defining the human deubiquitinating enzyme interaction landscape. *Cell* **138**, 389-403 (2009).
92. Hediyeh-Zadeh, S., Webb, A.I. & Davis, M.J. MsImpute: Estimation of Missing Peptide Intensity Data in Label-Free Quantitative Mass Spectrometry. *Mol Cell Proteomics* **22**, 100558 (2023).
93. Berg, S. et al. ilastik: interactive machine learning for (bio)image analysis. *Nat Methods* **16**, 1226-1232 (2019).
94. Perez-Riverol, Y. et al. The PRIDE database resources in 2022: a hub for mass spectrometry-based proteomics evidences. *Nucleic Acids Res* **50**, D543-D552 (2022).

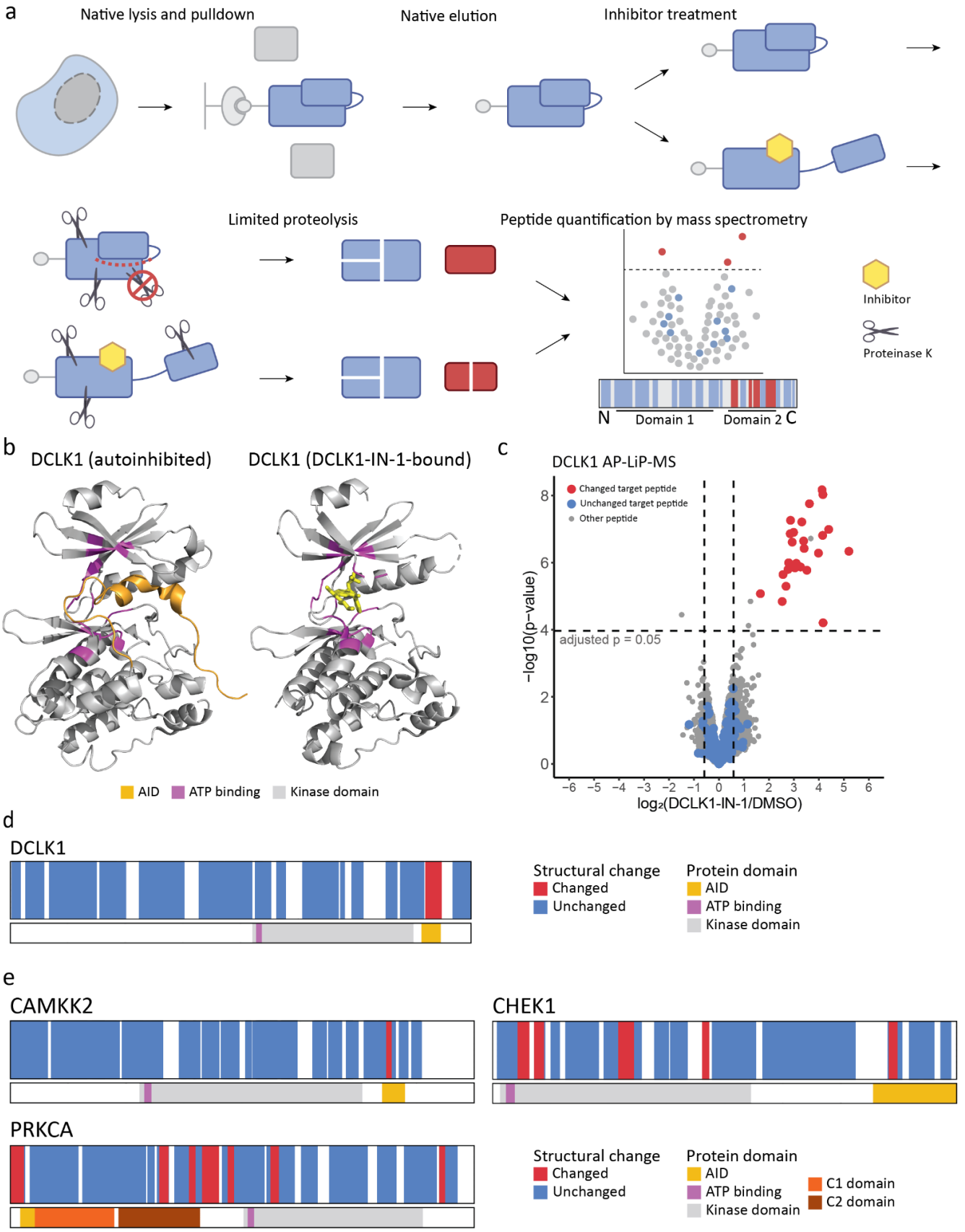

Fig. 1. Studying structural changes in response to inhibitor binding by AP-LiP-MS. a) Overview of the AP-LiP-MS workflow. Proteins were lysed and eluted under native conditions before the corresponding inhibitor was added. Following limited proteolysis with PK, the conformation-specific protein fragments were further digested with trypsin under denaturing conditions. Finally, peptides were measured by LC-MS/MS and compared across conditions. b) Comparison of the resolved structures of DCLK1 in the autoinhibited configuration (PDB: 6KYQ) and the DCLK1-IN-1 bound configuration (PDB: 7KXW; the inhibitor DCLK1-IN-1 is shown in yellow). c) Volcano plot showing LiP peptide intensity changes in the DCLK1-enriched samples upon treatment with DCLK1-IN-1 compared to vehicle control. In red are significantly changing DCLK1 peptides, in blue are the non-changing DCLK1

peptides. Peptides from other proteins are shown in grey. d) Barcode plot of structural changes in DCLK1 in response to inhibition with DCLK1-IN-1. e) Structural changes observed with AP-LiP-MS for CAMKK2 treated with SGC-CAMKK2-1, CHEK1 treated with rabusertib, and PRKCA treated with Gö 6983. All AP-LiP-MS experiments were performed in triplicates and p-values were calculated using a moderated t-test followed by multiple testing corrections using the procedure of Benjamini-Hochberg.

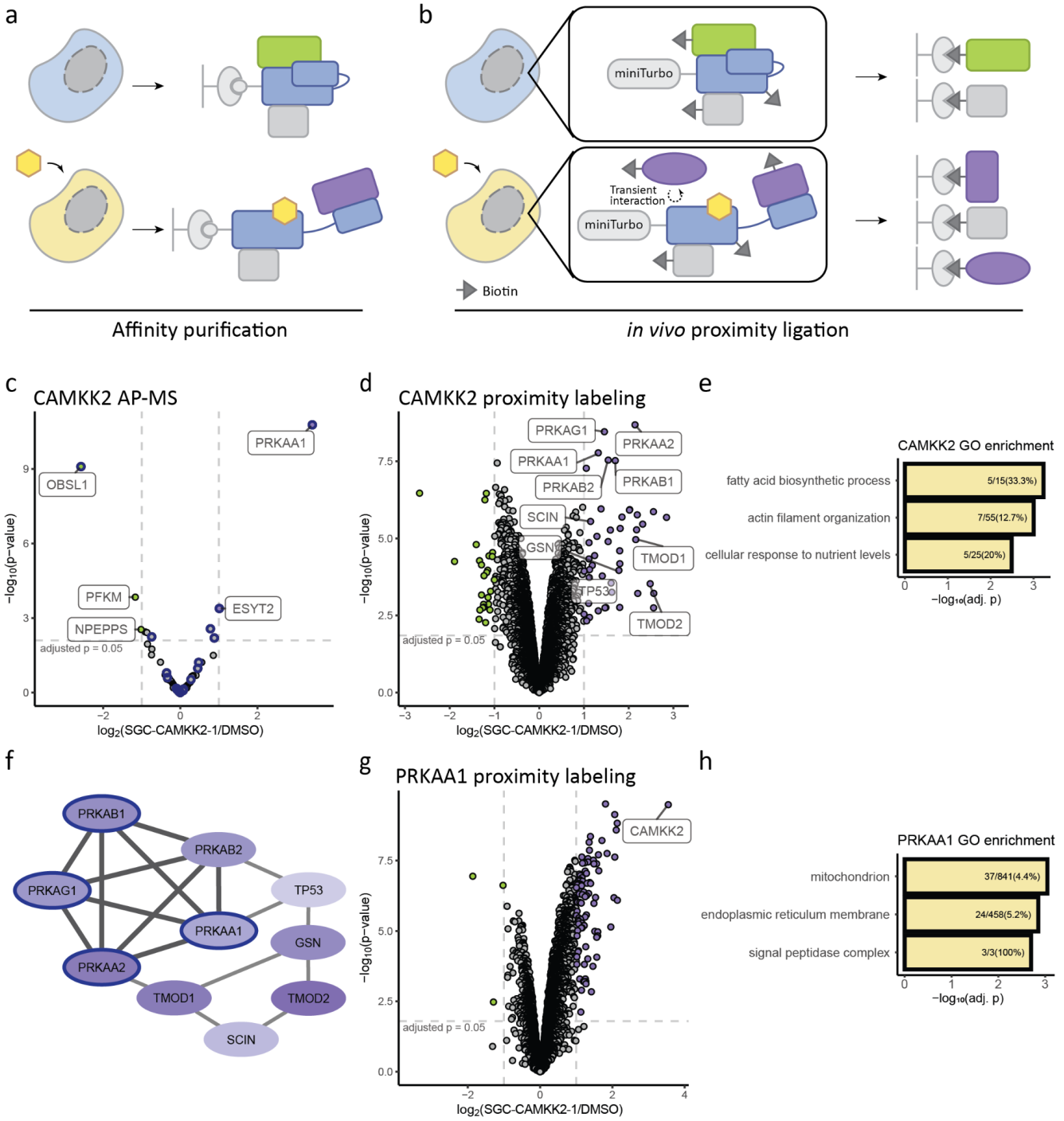

Fig. 2. Binding of the inhibitor SGC-CAMKK2-1 changes CAMKK2 complex formation and proximity. a) Illustration of the AP-MS workflow. b) Illustration of the *in vivo* proximity labeling workflow. c) Volcano plot illustrating changes in CAMKK2 interactors upon inhibition with SGC-CAMKK2-1 measured by AP-MS. Known CAMKK2 interactors are highlighted with a blue border. P-values were calculated using a moderated t-test followed by multiple testing corrections using the procedure of Benjamini-Hochberg. d) Changes in the proximity of CAMKK2 upon inhibition with SGC-CAMKK2-1. P-values were calculated using a moderated t-test followed by multiple testing corrections using the procedure of Benjamini-Hochberg. e) GO enrichment analysis (biological process) of the significantly changing proteins in panel d. P-values were calculated using a Fisher's exact test followed by multiple testing corrections using the procedure of Benjamini-Hochberg. f) PPI network showing the subunits of AMPK complexes and highly interconnected interactors that are significantly increased in the proximity of CAMKK2 upon treatment with SGC-CAMKK2-1 shown in panel d. The AMPK subunit interactions are highlighted with darker edges, and known interactors of CAMKK2 are outlined in blue. g) Reciprocal *in vivo* proximity labeling data showing changes in PRKAA1 proximity upon CAMKK2 inhibition. P-values were calculated using a moderated t-test followed by multiple testing corrections using the procedure of Benjamini-Hochberg. h) GO enrichment analysis (cellular component) of the significantly changing proteins in panel g. P-values were calculated using a Fisher's exact test followed by multiple testing corrections using the procedure of Benjamini-Hochberg. AP-MS experiments were performed in triplicates, and *in vivo* proximity labeling experiments in quadruplicates.

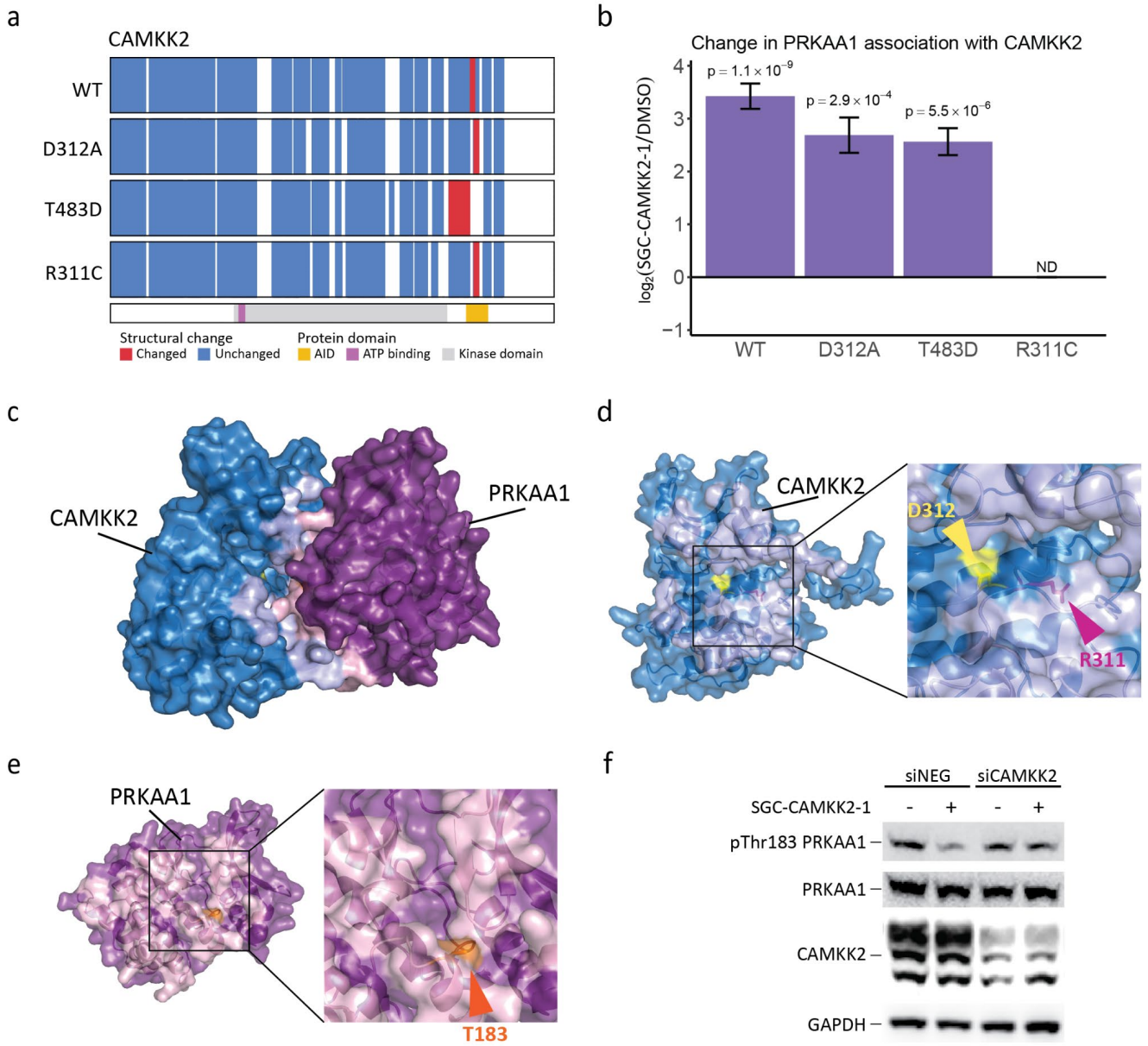

Fig. 3. Inhibitor-induced CAMKK2-PRKAA1 complex formation can attenuate T183 phosphorylation of PRKAA1 by other kinases. a) Comparison of structural changes in CAMKK2 mutants upon SGC-CAMKK2-1 treatment as measured by AP-LiP-MS. b) Bar graph representing $\log_2$(fold change) in PRKAA1 association with CAMKK2 wildtype and indicated mutants following SGC-CAMKK2-1 treatment as measured by AP-MS. Error bars represent the standard error of the mean of the $\log_2$(fold change). c) Predicted structure of the CAMKK2-PRKAA1 complex. CAMKK2 is shown in blue, and PRKAA1 is shown in purple and the predicted interfaces are highlighted in light blue and pink, respectively. Only kinase domains were used in the prediction. d) An up-close view of R311 and D312 of CAMKK2 at the CAMKK2-PRKAA1 interface. R311 is shown in magenta, and D312 is shown in yellow. The predicted interface is highlighted in light blue. e) The predicted PRKAA1 interface in the CAMKK2-PRKAA1 complex. The residue T183 is shown in orange, the predicted interface highlighted in pink. f) Western blot of PRKAA1 phosphorylation in response to CAMKK2 inhibition or siRNA mediated CAMKK2 knockdown. HEK293 cells were treated with control siRNA (siNEG) or siCAMKK2 for 48 hours and vehicle control or SGC-CAMKK2-1 for 4 hours as indicated. Cells were then subjected to glucose starvation for 20 minutes to induce T183 phosphorylation on PRKAA1. AP-LiP-MS and AP-MS experiments were performed in triplicates. P-values were calculated using a moderated t-test followed by multiple testing corrections using the procedure of Benjamini-Hochberg.

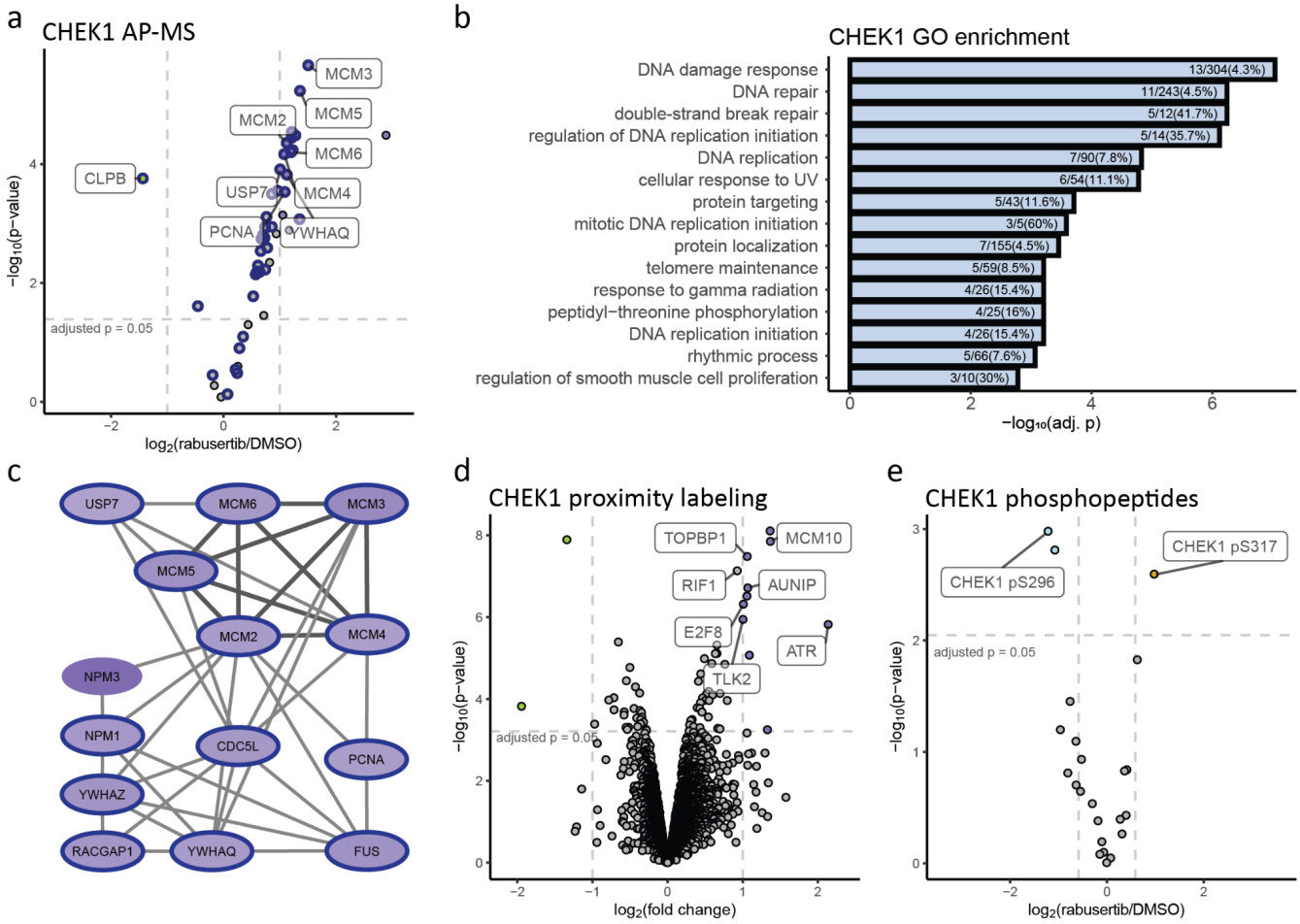

Fig. 4. Characterization of changes in CHEK1 complexes and proximity upon rabusertib treatment. a) Volcano plot illustrating changes in abundance of CHEK1 interactors in response to rabusertib identified by AP-MS. Known CHEK1 interactors are highlighted with a blue border. P-values were calculated using a moderated t-test followed by multiple testing corrections using the procedure of Benjamini-Hochberg. b) GO enrichment analysis (biological process) of all interactors of CHEK1 identified by AP-MS. P-values were calculated using a Fisher's exact test followed by multiple testing corrections using the procedure of Benjamini-Hochberg. c) A highly interconnected subnetwork of the proteins associating with CHEK1 upon rabusertib treatment measured in panel a. The MCM complex is highlighted with darker edges, and known interactors of CHEK1 are highlighted with a blue border. d) Changes in the proximity of CHEK1 upon inhibition with rabusertib. P-values were calculated using a moderated t-test followed by multiple testing corrections using the procedure of Benjamini-Hochberg. e) Changes in phosphorylation upon CHEK1 inhibition with rabusertib extracted from AP-MS results. P-values were calculated using a moderated t-test followed by multiple testing corrections using the procedure of Benjamini-Hochberg. AP-MS experiments were performed in triplicates, and *in vivo* proximity labeling experiments in quadruplicates.

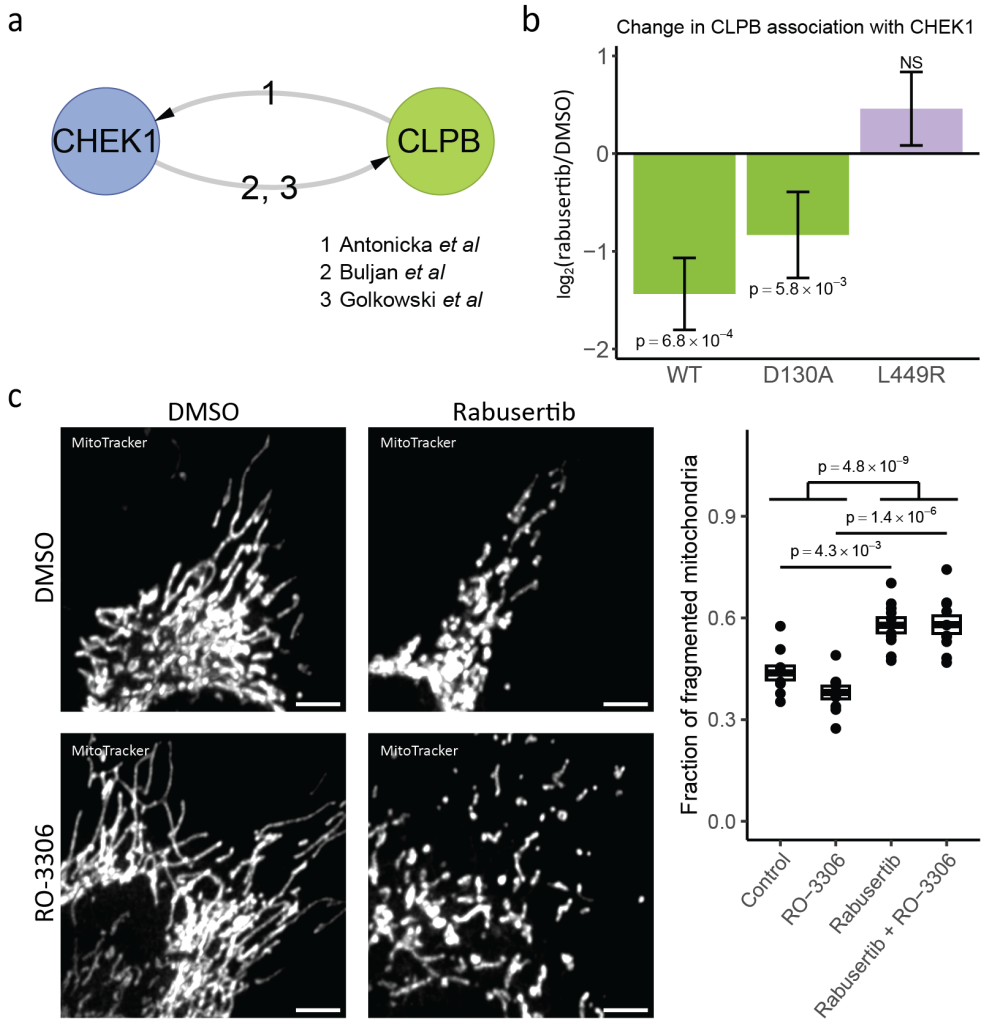

Fig. 5. Rabusertib disrupts CHEK1-CLPB complex formation and causes mitochondrial fragmentation. a) Previous studies detecting CHEK1-CLPB complex. b) Bar graph representing $\log_2$(fold change) in CLPB association with CHEK1 WT and indicated mutants upon rabusertib treatment. Error bars represent the standard error of the mean of the $\log_2$(fold change). P-values were calculated using a moderated t-test followed by multiple testing corrections using the procedure of Benjamini-Hochberg. Experiments were performed in triplicates. c) Super-resolution microscopy of mitochondria in HeLa cells treated with rabusertib in the presence and or absence of RO-3306. Images were segmented and mitochondria were classified based on their morphology as either fragmented or elongated. Within each image, the area of fragmented mitochondria was normalized by the total area of detected mitochondria. P-values were calculated by ANOVA followed by Tukey HSD. For each condition, 10 images taken across 3 replicates were quantified. The scale bars represent 5 µm.

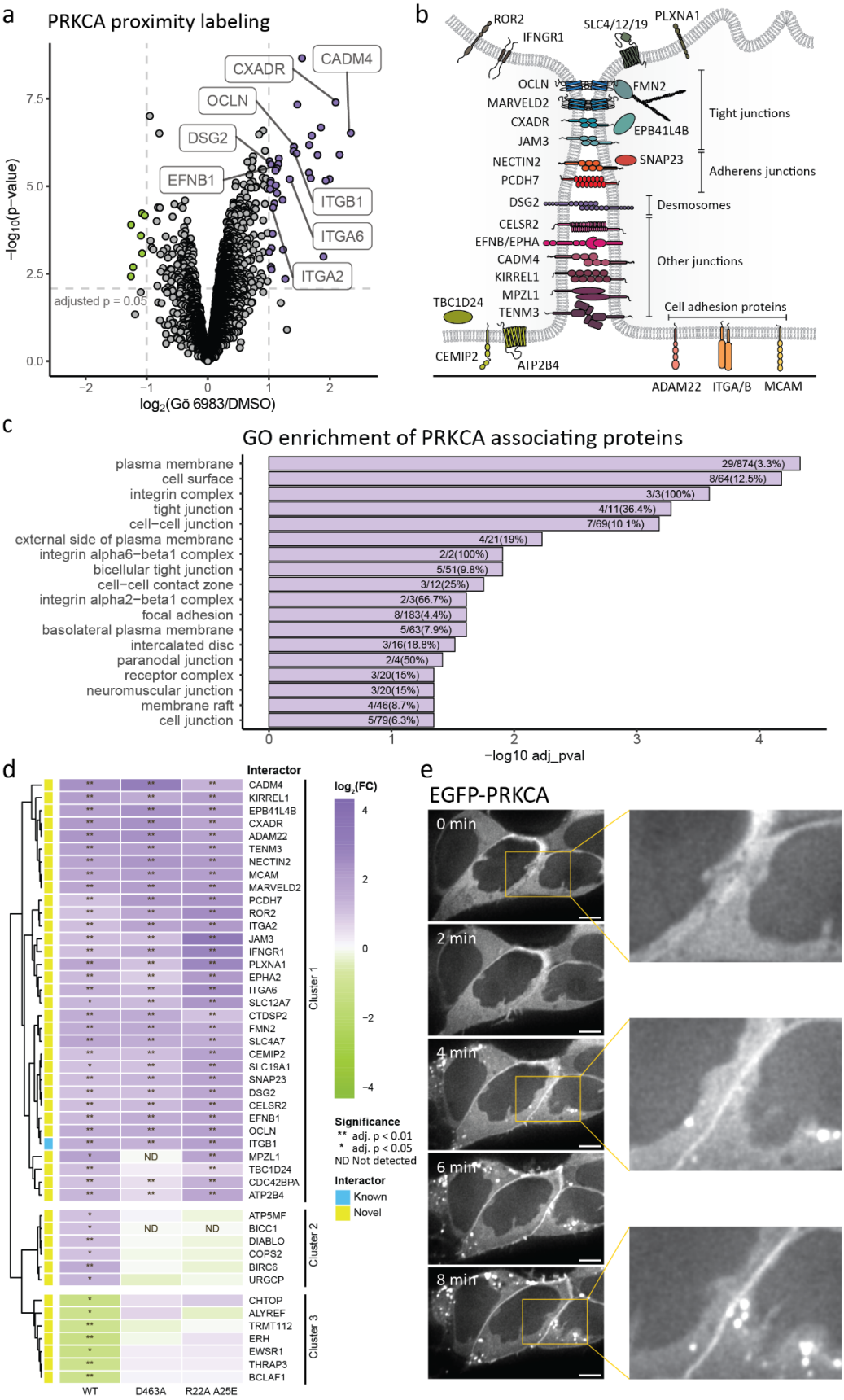

Fig. 6. Membrane relocalization of PRKCA upon Gö 6983 treatment. a) Changes in the proximity of PRKCA upon inhibition with Gö 6983. P-values were calculated using a moderated t-test followed by multiple testing corrections using the procedure of Benjamini-Hochberg. b) Illustration of the proteins annotated with GO terms 'plasma membrane' or 'cell adhesion' found increased in proximity to PRKCA upon Gö 6983 treatment. c) GO enrichment analysis (cellular component) of proteins associating with PRKCA upon Gö 6983 treatment. P-values were calculated using a Fisher's exact test followed by multiple testing corrections using the procedure of Benjamini-Hochberg. d) Comparison of proximity changes upon Gö 6983 treatment in PRKCA WT, the catalytically inactive D463A mutant and the active R22A/A25E double mutant. P-values were calculated using a moderated t-test

followed by multiple testing corrections using the procedure of Benjamini-Hochberg. e) Super-resolution live-cell microscopy of HEK293 cells expressing EGFP-PRKCA upon Gö 6983 treatment. The scale bars represent 5 μm.